



**Measurement and modeling of
adsorptive–poromechanical properties of bituminous
coal cores exposed to CO₂: Adsorption, swelling strains,
swelling stresses and impact on fracture permeability**

D.N. Espinoza, Matthieu Vandamme, Jean-Michel Pereira, Patrick Dangla, S.
Vidal-Gilbert

► **To cite this version:**

D.N. Espinoza, Matthieu Vandamme, Jean-Michel Pereira, Patrick Dangla, S. Vidal-Gilbert. Measurement and modeling of adsorptive–poromechanical properties of bituminous coal cores exposed to CO₂: Adsorption, swelling strains, swelling stresses and impact on fracture permeability. *International Journal of Coal Geology*, 2014, 134-135, pp.80-95. 10.1016/j.coal.2014.09.010 . hal-01118563

HAL Id: hal-01118563

<https://hal.science/hal-01118563>

Submitted on 10 May 2019

HAL is a multi-disciplinary open access archive for the deposit and dissemination of scientific research documents, whether they are published or not. The documents may come from teaching and research institutions in France or abroad, or from public or private research centers.

L'archive ouverte pluridisciplinaire **HAL**, est destinée au dépôt et à la diffusion de documents scientifiques de niveau recherche, publiés ou non, émanant des établissements d'enseignement et de recherche français ou étrangers, des laboratoires publics ou privés.

Measurement and modeling of
adsorptive-poromechanical properties of bituminous coal
cores exposed to CO₂: adsorption, swelling strains,
swelling stresses and impact on fracture permeability

D. N. Espinoza^{a,b}, M. Vandamme^a, J. -M. Pereira^a, P. Dangla^a, S.
Vidal-Gilbert^c

^a*Université Paris-Est, Laboratoire Navier, (UMR 8205), ENPC, CNRS, IFSTTAR*

^b*The University of Texas at Austin, Department of Petroleum and Geosystems
Engineering*

^c*Total S.A., Unconventional Gas Resources*

Abstract

The reservoir response of unmineable coal seams to primary and enhanced natural gas recovery is strongly affected by the gas sorption and swelling properties of the coal reservoir rock. In-depth understanding of the process of gas sorption/desorption in the coal matrix, induced deformation and measurement of relevant physical parameters are critical for predictive reservoir management. Models used in industry practice are based on swelling strains measured in “free” swelling coal or on empirical correlations between strain and adsorption, and predict permeability changes based on changes of porosity or stress calculated assuming an analogy with thermoelasticity. However, not only coal seams are subjected to in-situ stresses and geometrical boundary conditions but also sorption and strain are strongly coupled. Representative experiments and a truly coupled model for coal seams are needed in challenging applications. We present a set of triaxial testing mea-

surements on 38 mm diameter fractured sub-bituminous/bituminous coal cores exposed to CO₂. Testing includes the measurement of fluid uptake, adsorption-induced strains and stresses, and the impact on simultaneously measured permeability. Noteworthy, we measured increases in effective stress of up to 29 MPa when injecting CO₂ at 5 MPa and preventing the coal core to swell. The results are analyzed with a poromechanical model in which coal matrix microporosity and adsorption-induced phenomena are embedded into a fractured reservoir rock with transverse isotropic properties. The adsorption-mechanical coupling in the coal matrix is integrated through an adsorption stress function and fractured coal permeability is estimated as a function of Terzaghi's effective stresses (parallel and perpendicular to the bedding plane). The experimental results and model predictions help identify the characteristic response of coal microporosity and cleat macroporosity on the poromechanical response of coal cores, and suggest that the order of magnitude change of reservoir permeability observed in the field are linked to sorption-induced change on Terzaghi's effective horizontal stress under laterally constrained displacement condition. Together, the modeling and experimental characterization offer unprecedented insights into the mechanics of coal.

Keywords: sorption, CBM, unconventional, natural fractures, nanoporosity, chemo-mechanical coupling

1. Introduction

Currently, natural gas accounts for roughly 21% of the World's energy supply, being coal-bed methane an important contributor in countries such

as Australia, USA, Canada, and China (IEA, 2013; EIA, 2013). Natural gas production from coal beds is expected to increase as more reservoirs are discovered and technology enables enhanced production. Coal beds may also contribute to storing and sequestering geologically CO₂, conceivable up to 20 GtCO₂ (Gale, 2004).

Various characteristics make coal beds a unique geomaterial, showing poromechanical properties notably different from other reservoir rocks:

(1) Coal seams are naturally fractured reservoirs. Diagenetic processes lead to opening mode fractures predominantly oriented perpendicular to the bedding plane, called cleats (Laubach et al., 1998). Cleats compose most of the macroporosity, where fluid advection takes place (Mazumder et al., 2006; Pan and Connell, 2007). The presence of cleats induces hydro-mechanical anisotropy to the rock properties (Hu et al., 2010).

(2) At the smallest scale, coal seams are constituted by a microporous disordered organic continuum, which we call from now on the coal matrix. Micropores sized in the order of 10^{-9} m compose the coal microporosity. The coal matrix can also host mesopores sized in the order of 10^{-8} m. The coal matrix is capable of adsorbing various gases including CO₂, CH₄, and N₂, which lead to coal matrix volumetric swelling in the order of few percents upon adsorption (Reucroft and Sethuraman, 1987; Ceglarska-Stefanska and Czaplinski, 1993; Levine, 1996; Mazumder et al., 2006; Pan and Connell, 2007; Pini, 2009). Conversely, desorption leads to coal matrix shrinkage. Overburden and bedding processes add anisotropy to the coal matrix properties (Cody et al., 1988; Hol and Spiers, 2012; Espinoza et al., 2013). Within the coal matrix, fluid transport occurs by a combination of diffusion and slow advection

(Ceglarska-Stefanska and Zarebska, 2002).

The variety of pore sizes in coal seams yields various types of fluid pore habit. Macropores host fluids mostly in bulk conditions. Mesopores host fluids in adsorbed state near solid walls and in bulk state far from solid walls. Micropores contain fluids just in adsorbed state, sometimes called “dissolved” fluid in the solid matrix. Additional fluids may be present as solutes in the water phase.

Sorption-induced swelling has an important effect on coal seam permeability (Pan and Connell, 2012). Changes of more than two orders of magnitude in permeability have been observed (1) during primary methane production – permeability increase due to desorption-induced shrinkage and cleat opening (Palmer and Mansoori, 1998; Scott et al., 2012) and (2) during CO₂ injection – permeability decrease due to adsorption-induced swelling and cleat closing (Pekot and Reeves, 2002; Oudinot et al., 2011). Such a unique behavior of coal has led to the development of semi-empirical models and poromechanical models to account for the adsorption-strain coupling developed in microporous coal matrix and predict its impact on seam permeability (Palmer and Mansoori, 1998; Shi and Durucan, 2004; Cui et al., 2007; Wu et al., 2010; Vandamme et al., 2010; Pijaudier-Cabot et al., 2011; Brochard et al., 2012; Nikoosokhan et al., 2012, 2014).

Coal seam coupled reservoir simulation seeks to predict the evolution of permeability as a function of bottomhole pressure. The relevant parameters include cleat compressibility, mechanical moduli and a measurement that can account for the swelling properties of coal. Current industry codes use swelling strains (making an analogy with thermoelasticity) in order to couple

the effects of sorption on the variation of in-situ stress and porosity with depletion. These parameters are usually obtained from laboratory testing and field data history matching.

Studies of adsorption in coal cores and ensuing change in permeability are scarce because of several reasons including difficulty in coring fractured coal and obtaining representative coal samples, long time required to reach adsorption thermodynamic equilibrium, influence of confining stress on permeability as a rate-limiting factor for CO₂ delivery into coal matrix micropores, and need for special non-adsorbing membranes and sealing o-rings. Salient observations from selected experimental studies follow (Czaplinski and Holda, 1982; Levine, 1996; Chikatamarla et al., 2004; Mazumder et al., 2006; Viete and Ranjith, 2006; Day et al., 2008; Pini, 2009; Pone et al., 2009; Hagin and Zoback, 2010; Pan et al., 2010; Hol et al., 2012; Masoudian et al., 2013, 2014): (1) CO₂ equilibration times increase as the specimen size increases and vary from about 1 hour to more than 20 days, (2) swelling along the direction perpendicular to the bedding plane is generally higher –up to 60%– than along the direction parallel to the bedding plane, (3) absolute permeability decreases with Terzaghi’s effective stress at a given fluid pressure, however, the variation of permeability as a function of pressure of the adsorbate fluid at constant Terzaghi’s effective stress is not clear, and (4) CO₂ sorption in coal lowers –up to 25%– the Young’s modulus and shear strength and enhances creep, compared to dry coal or coal saturated with helium.

The objective of this study is to measure the coupled poromechanical response and permeability of coal cores injected with an adsorbate under

different loading and strain boundary conditions, interpret the results in the context of a double porosity model for transverse isotropic fractured microporous solids (fully coupled regarding fluid mass, fluid pressure, and solid stress), and give insight into the evolution of permeability of the coal seam in-situ during primary and secondary methane recovery.

2. Double porosity model for transverse isotropic fractured coal

2.1. Poromechanical model

We present a poromechanical model for double porosity transverse isotropic reservoirs rocks. An isotropic version of this model is found elsewhere (Nikoosokhan et al., 2012, 2014). The double porosity system is composed by (1) the cleat macroporosity where the fluid can be modeled as in bulk conditions with a proper equation of state, and (2) the microporosity where adsorption takes place, fluid behavior deviates from bulk conditions, and adsorptive-mechanical coupling develops (swelling or shrinkage). The influence of cleat compressibility (natural fractures) on the behavior of the fractured coal is modeled with conventional anisotropic poroelasticity (Cheng, 1997; Coussy, 2004; Cowin, 2004) and the effect of adsorption-induced phenomena on the coal matrix is modeled with the theory of poromechanics for microporous media developed by Brochard et al. (2012). Appendix A details the model derivation. The following set summarizes the equilibrium, porosity, and mass balance equations for a cartesian representative elementary volume (REV) of fractured coal with transverse isotropy around axis 3 (See Figure 1):

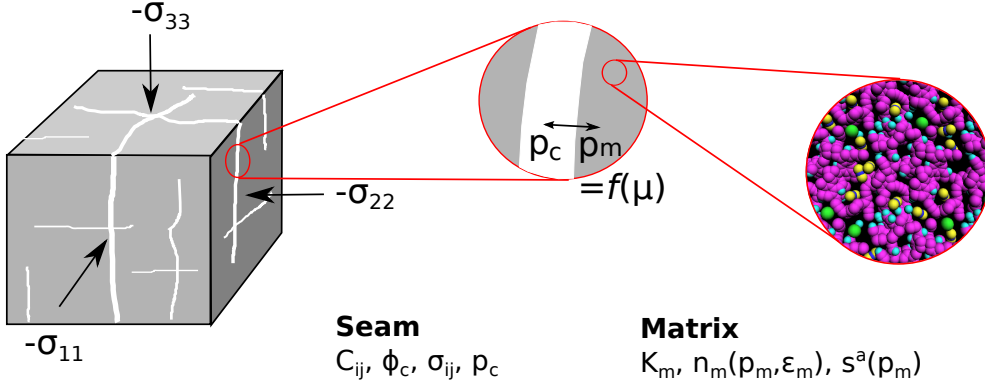


Figure 1: Representative elementary volume of fractured coal and relevant modeling parameters. Fracture zoom sketches the interplay between pressure p_c of bulk fluid in the cleats, and thermodynamic pressure p_m of fluid in the coal matrix. Coal matrix zoom shows a molecular representation of coal and adsorbed fluid molecules (Courtesy: L. Brochard).

$$\left\{ \begin{array}{l} \sigma_{11} = C_{11}\varepsilon_{11} + C_{12}\varepsilon_{22} + C_{13}\varepsilon_{33} - b_1 p_c - (1 - b_1)s^a(p_m) \\ \sigma_{22} = C_{12}\varepsilon_{11} + C_{11}\varepsilon_{22} + C_{13}\varepsilon_{33} - b_1 p_c - (1 - b_1)s^a(p_m) \\ \sigma_{33} = C_{13}\varepsilon_{11} + C_{13}\varepsilon_{22} + C_{33}\varepsilon_{33} - b_3 p_c - (1 - b_3)s^a(p_m) \\ \sigma_{23} = 2C_{44}\varepsilon_{23} \\ \sigma_{31} = 2C_{44}\varepsilon_{31} \\ \sigma_{12} = 2\frac{C_{11}-C_{12}}{2}\varepsilon_{12} \\ \phi_c - \phi_{c0} = [p_c - s_a(p_m)]/N + b_1(\varepsilon_{11} + \varepsilon_{22}) + b_3\varepsilon_{33} \\ n_T = (1 - \phi_{c0})n_m(p_m, \varepsilon_m) + \phi_c \rho_b \end{array} \right. \quad (1)$$

The first six equations capture the fractured coal stress tensor including fracture poroelastic effects and adsorption stresses from the coal matrix. Equations indicate that the fractured coal mechanical deformational behavior depends on the five independent stiffness coefficients C_{11} , C_{12} , C_{13} , C_{33} , C_{44} of the fractured coal (include effect of fracture compressibility), the poromechanical coupling depends on the fracture-induced Biot coefficients (b_1 , b_3) of the fractured coal (Equation A.20) and the adsorptive-mechanical coupling

depends on the pressure-dependant adsorption stress developed by the coal matrix $s^a(p_m)$. The adsorption stress quantifies the swelling potential of the coal matrix, it is considered isotropic here and it is equivalent to the stress that should be applied to a specimen of coal matrix exposed to an adsorbate at pressure p_m not letting it develop swelling strains. The adsorption stress can be measured experimentally at the scale of the tested specimen. Our model predicts its value based on the amount of adsorbed fluid n_m , the adsorption-strain coupling coefficient $c(p_m)$, and the coal matrix bulk modulus K_m (Eq. A.10). The seventh equation allows calculating the cleat porosity ϕ_c as a function of the initial porosity ϕ_{c0} , the poroelastic coefficient N (Eq. A.20), the strains of fractured coal ε_{ij} , cleat pressure p_c , and adsorption stress $s^a(p_m)$. The eighth equation permits obtaining the total amount of fluid in the fractured coal per unit volume of fractured coal n_T as sum of the amount of fluid sorbed in the matrix n_m (as a function of pressure p_m and volumetric strain ϵ_m of the coal matrix – first term) and the amount of fluid in the cleats (which depends on cleat porosity ϕ_c and bulk fluid molar density ρ_b –second term). The coal matrix strain is given by Equation (A.5). The total amount of sorption in the coal matrix n_m is modeled assuming a Langmuir isotherm (parameters n_0^{max} , p_{L0}), and a first-order expansion respect to coal matrix strain with a proportionality factor termed adsorption-strain coupling coefficient $c(p_m)$ (Equation A.3). The coal matrix is assumed isotropic with bulk modulus K_m (the origin of anisotropy is discussed in Section 5.2.1). Thus, the full double porosity model has 10 independent parameters, six of them defined at the fractured coal scale and four at the coal matrix scale.

Non-sorbing and non-swelling rocks have negligible adsorption $n_m(p_m, \epsilon_m) = 0$ and adsorption stress $s^a(p_m) = 0$. In this case Equation (1) simplifies to conventional transverse poroelasticity (Equation A.19). Coal is able to sorb different gases with ensuing swelling. The value of $n_m(p_m, \epsilon_m)$ is in the order of 1 mol/L and adsorption stresses s^a reach several tens of MPa (Brochard et al., 2012; Espinoza et al., 2013).

2.2. Stress-permeability empirical relationship

Stress-based models correlate the logarithm of permeability to stresses, e.g., the mean Terzaghi's effective stress $\sigma' = -(\sigma + p)$, or to the horizontal Terzaghi's effective stress $\sigma'_h = -(\sigma_h + p)$ (Somerton et al., 1975; Shi and Durucan, 2004; Cui et al., 2007; Pan and Connell, 2012). In the line of previous work (Seidle et al., 1992; Connell et al., 2010; Wu et al., 2010), we adopt a permeability which depends on Terzaghi's effective stress and considers independently parallel to bedding and perpendicular to bedding stresses through permeability fracture compressibility coefficients α_{\parallel} and α_{\perp} respectively, such that,

$$k = k_0 \exp [\alpha_{\parallel}(\sigma'_{\parallel} - \sigma'_{\parallel 0}) + \alpha_{\perp}(\sigma'_{\perp} - \sigma'_{\perp 0})] \quad (2)$$

where k_0 is the reference permeability at a reference state $(\sigma_{\parallel 0}, \sigma_{\perp 0}, p_{c0}, s^a(p_{m0}))$. This equation only accounts for the stress-sensitive part of fracture permeability and disregards horizontal stress anisotropy and shear-enhanced permeability.

3. Coal core triaxial testing

3.1. Coal characterization

The tested coal comes from Forzando mine in South Africa, at an original depth of ~ 500 m. The recovered coal block (about $\sim 1\text{m}^3$) shows high degree of fracturing with predominant orthogonally intersecting cleats, many of them filled with calcite. Thin layers of clay mixed with the coal matrix are visible in several sections. Vitrinite reflectance equal to 0.57% classify this coal as sub-bituminous A/high volatile C bituminous (ASTM D 388). Several cores were drilled in directions perpendicular and parallel to the bedding plane (Figure 2). Specimens showed little damage during coring. Selected specimens have been subjected to X-ray microtomography to investigate the degree of specimen fracturing and fractures orientation. Figure 2 shows tomographic cross sections obtained in direction perpendicular to the bedding plane. Empty cleats are seen as black regions while calcite-filled cleats are imaged in white. Some empty cleats may be artifacts due to sample recovery and coring.

The bulk density of cores ranges from 1318 to 1356 kg/m^3 (See Table 1). The mass density of the coal skeleton is about $\rho_m = 1510 \text{ kg/m}^3$ as measured by the accessible helium void volume. The combination of these two measurements indicates specimen total helium porosity (fracture and microporosity) ranging from ~ 11.3 to 13.9% . SEM imaging performed on 1 cm diameter coal cores shows the presence of microfractures ranging from 50 μm to less than 1 μm . Figure 3-a shows a calcite-filled fracture with total aperture 50 μm being intercepted at $\sim 90^\circ$ by a smaller 10 μm empty fracture. We measured pore size distribution with a mercury intrusion porosime-

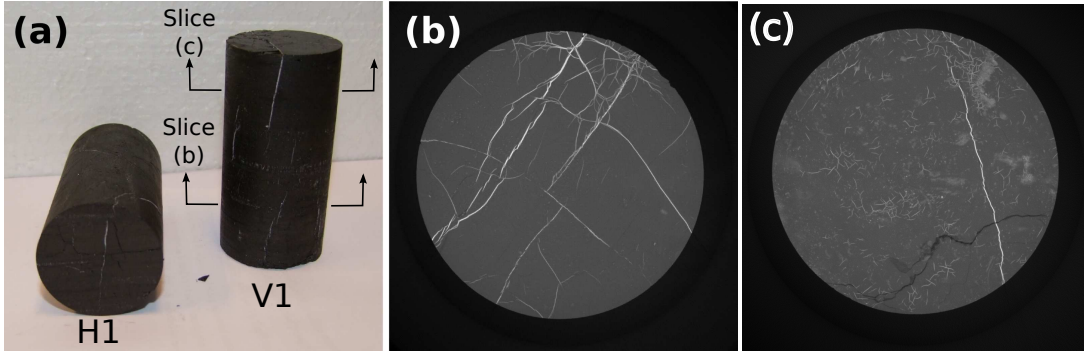


Figure 2: Coal cores 38 mm diameter – slenderness ratio 2:1 used for triaxial tests. (a) Cores picture: coring parallel to the bedding plane (left); coring perpendicular to the bedding plane (right). (b-c) X-ray tomographic reconstruction of cross sections on the bedding plane (image resolution 25 μm - performed at Laboratoire Navier <navier.enpc.fr/Microtomographie>).

ter Micromeritics-Autopore IV on a coal specimen of $\sim 1 \text{ cm}^3$ volume with a crack barely observable without magnification. Maximum mercury penetration at 207 MPa (equivalent to pore size $\sim 6 \text{ nm}$) shows a maximum cumulative intrusion volume of 0.031 mL/mL (Figure 3-b). The incremental pore volume curve (derivative of data in Figure 3) shows that most of the mercury-intruded porosity in this small sample is composed by either pores smaller than 60 nm or bigger than 10 μm . Elevated mercury pressure may compress the coal matrix, collapse non-invaded pores, and overestimate microporosity. Independent low-pressure nitrogen adsorption measurements on coal crashed from the same seam suggest a peak of pore size distribution at 40 nm. The Auxiliary Material shows excess sorption measurements on crushed coal from the same coal seam (performed by BGC-Analytik UG).

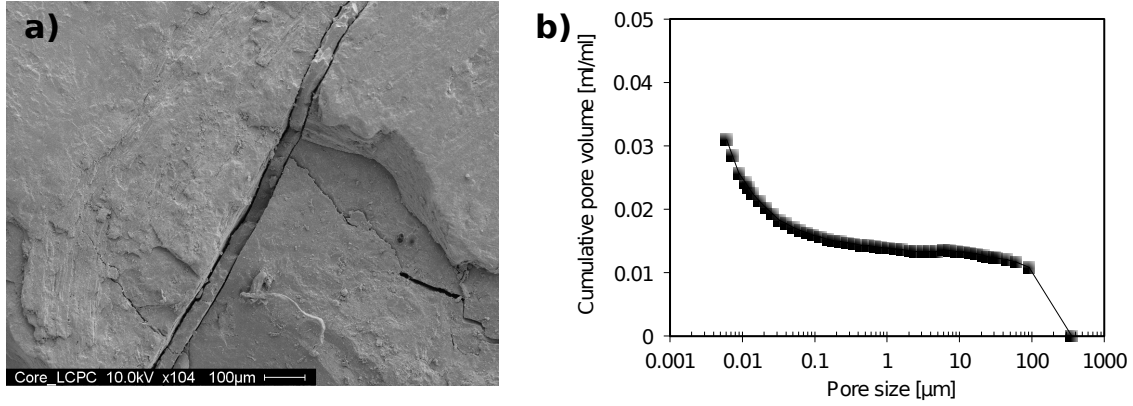


Figure 3: Coal characterization. (a) SEM imaging on a partially calcite-filled fracture. (b) Mercury intrusion porosimetry on a $\sim 1 \text{ cm}^3$ coal sample.

3.2. Triaxial cell

The experimental apparatus is designed to (1) measure core axial and radial deformations, (2) control independently axial and radial stresses, (3) measure CO_2 uptake by the coal specimen, and (4) measure core permeability. The following summarizes the triaxial cell characteristics and operation range. Sanchez Technologies manufactured the triaxial cell (Model: Tr-X 40/60) and provided the fluid pumps. Figure 4 shows a schematic representation of the triaxial cell.

Specimen. The triaxial cell fits cylindrical specimens 38 mm (1.5 in) diameter and slenderness 2:1. This specimen size permits accommodating several submillimeter-sized cleats.

Stresses. Pressurized silicone oil applies the radial stress (40 MPa maximum), and a pressure-driven piston applies the axial stress (60 MPa maximum).

Pore Fluid System. The CO_2 pore fluid system is managed by upstream and downstream syringe pumps. The first pump injects and measures CO_2

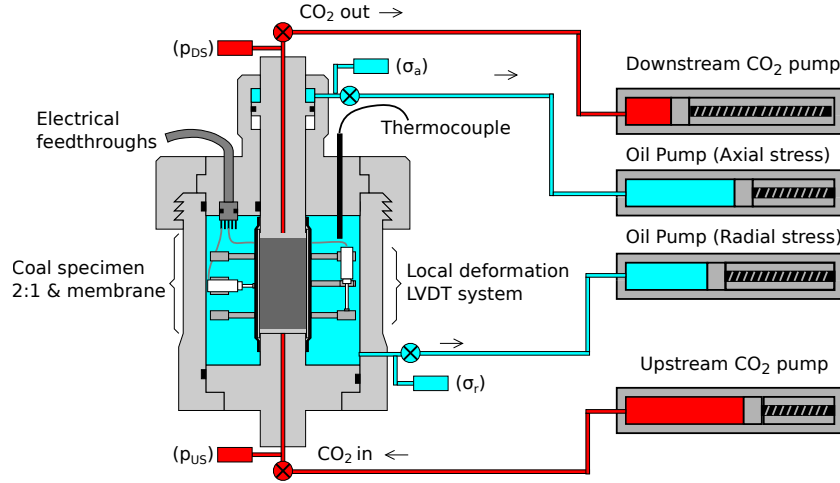


Figure 4: Experimental triaxial device. Main characteristics include: maximum radial stress 40 MPa, maximum axial stress 60 MPa, measurement of local strains, temperature control, and ability to handle supercritical CO₂.

flow rate and injection volume; the second pump controls CO₂ back-pressure. Stainless steel porous plates help distribute evenly the gas on the base and top faces of the specimen. A CO₂-resistant membrane combining layers of teflon and nitrile isolates the CO₂-saturated coal specimen from the surrounding confining fluid.

Strain Measurement. The device includes a specially designed system of displacement transducers (LVDT) to measure local radial and axial strains (three LVDTs for radial measurement and two LVDTs for axial measurements - 1 μm precision manufactured by Solartron - see details in Monfared et al. 2011).

Temperature. Two internal thermocouples measure the temperature of the confining fluid. Electrically-powered heating jackets control specimen and CO₂ pumps temperature. The maximum working temperature is 60°C.

Wiring, Acquisition, and Control. Electrical feedthroughs let measure output electrical signals from transducers placed inside the triaxial cell.

Table 1: List of performed triaxial experiments including their main characteristics. The experimental testing program includes cores drilled perpendicular \perp and parallel \parallel respect to the bedding plane. Coal specimens have a gravimetric water content 2 to 3%. Helium porosity is estimated with the helium skeletal mass density 1510 Kg/m³.

Specimen	Bulk mass density ρ_b [kg/m ³]	Helium porosity [%]	Type of dry loading	Stress/strain condition during CO ₂ injection	Stress/strain condition during permeability test
V1(\perp)	1356	11.2	Anisotropic	Constant stress Constant volume	Changing effective stresses Constrained adsorption
V2(\perp)	1346	12.6	Anisotropic	Constant stress	-
V3(\perp)	1331	13.2	Anisotropic	Constant stress Constant volume	- -
H1(\parallel)	1351	12.3	Anisotropic	Constant stress	-
H2(\parallel)	1318	14.4	Anisotropic	Constant stress	-

Sanchez Technologies provided an electronic acquisition and control system.

Cell calibration. We calibrated the cell with an aluminum specimen to assess end-effects and pressure effects on the cell volume, and measure the compressibility of the nitrile membrane.

4. Experimental results and poromechanical model validation

The objective of the experimental work is to measure the adsorptive, mechanical and transport properties of coal at the core scale to evaluate the developed model as an analytical and predictive tool. Sections 4.1 to 4.3 deal with the measurement of adsorptive-mechanical parameters and poromechanical model validation. Section 4.4 adds steady-state permeability measurements and makes use of the previously developed model to predict

permeability upon adsorption in displacement constrained coal samples (near constant volume condition). All experiments are performed at a temperature $39 \pm 1^\circ\text{C}$, and specimens are vacuumed before testing. Table 1 presents a summary of the performed experiments.

Let us begin by considering a conceptual core drilled perpendicular to the bedding plane, such that, the axis of the cylindrical core aligns with the axis of material symmetry (assumed here perpendicular to the bedding plane) and with the axis of the cylindrical triaxial device (axis 3 - Figure 5). The principal stresses in directions parallel to the bedding plane are $\sigma_{11} = \sigma_{22} = \sigma_r$ and the principal stress in the direction perpendicular to the bedding plane is $\sigma_{33} = \sigma_a$. These loading conditions impose equal lateral strains $\varepsilon_{11} = \varepsilon_{22} = \varepsilon_r$, to the idealized transverse isotropic coal. The coupled equations (1) reduce to the following set

$$\begin{cases} \sigma_r &= (C_{11} + C_{12})\varepsilon_r + C_{13}\varepsilon_a - b_1p_c - (1 - b_1)s^a(p_m) \\ \sigma_a &= 2C_{13}\varepsilon_r + C_{33}\varepsilon_a - b_3p_c - (1 - b_3)s^a(p_m) \\ \phi_c - \phi_{c0} &= [p_c - s_a(p_m)]/N + 2b_1\varepsilon_r + b_3\varepsilon_a \\ n_T &= (1 - \phi_{c0})n_m(p_m, \epsilon_m) + \phi_c\rho_b \end{cases} \quad (3)$$

Strains as a function of stresses, fracture pore pressure, and adsorption stress result in

$$\begin{bmatrix} \varepsilon_r \\ \varepsilon_a \end{bmatrix} = \begin{bmatrix} \frac{1-\nu}{E} & -\frac{\nu_3}{E_3} \\ -2\frac{\nu_3}{E_3} & \frac{1}{E_3} \end{bmatrix} \begin{bmatrix} \sigma_r + b_1p_c + (1 - b_1)s^a(p_m) \\ \sigma_a + b_3p_c + (1 - b_3)s^a(p_m) \end{bmatrix} \quad (4)$$

Analogous equations can be developed from Equation (1) for cores drilled parallel to the bedding plane and loaded in a cylindrical triaxial device.

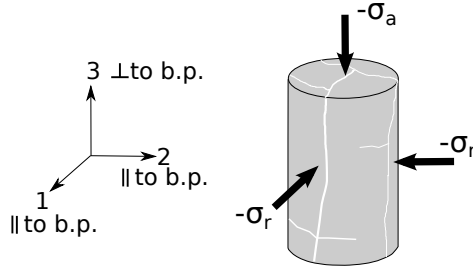


Figure 5: Coal core drilled perpendicular to the bedding plane (b.p.). The triaxial device applies axial stress σ_a and radial stress σ_r which correspond in this case to the seam stresses perpendicular and parallel to the bedding plane respectively.

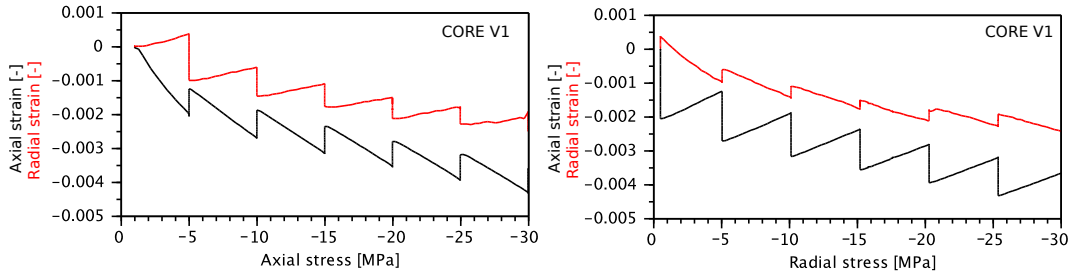


Figure 6: Strain-stress response to drained loading of coal core V1 in dry conditions - no CO_2 in pores. Loading is performed in 5 MPa stress increments (compressive stresses and contraction strains are negative).

4.1. Elastic moduli of dry coal specimens

Anisotropic loading is applied by steps with increasing axial stress σ_a at constant radial stress σ_r , and subsequently with increasing radial stress at constant axial stress. The loading is performed in drained conditions without CO_2 (no pressure build-up). Figure 6 shows dry loading stress-strain results from coal core V1.

The stress-strain data on cores drilled perpendicular to the bedding plane lets us recover directly three of the five elastic parameters (E_3 , ν_3 , $E/(1-\nu)$)

for linear transverse isotropic elasticity (from Equation 4):

$$\begin{cases} \left. \frac{\partial \varepsilon_r}{\partial \sigma_r} \right|_{p_c, p_m, \sigma_a} = \frac{1-\nu}{E} & ; \quad \left. \frac{\partial \varepsilon_r}{\partial \sigma_a} \right|_{p_c, p_m, \sigma_r} = -\frac{\nu_3}{E_3} \\ \left. \frac{\partial \varepsilon_a}{\partial \sigma_r} \right|_{p_c, p_m, \sigma_a} = -\frac{2\nu_3}{E_3} & ; \quad \left. \frac{\partial \varepsilon_a}{\partial \sigma_a} \right|_{p_c, p_m, \sigma_r} = \frac{1}{E_3} \end{cases} \quad (5)$$

Stress-strain data from cores drilled parallel to the bedding plane let us recover directly the elastic parameter E . Figure 7 shows the summary of tangent elastic moduli measured for all specimens as a function of axial and radial stresses. Young's elastic moduli values range from ~ 2 to 6 GPa in the range of confining stresses 0.5 to 30 MPa (Figure 7). Core specimens show non-negligible stress-strain nonlinearity, which reduces at confining stresses higher than 15 MPa. Fitting curves represent average stress-dependent elastic moduli values that will be used later to estimate secant moduli relevant to the range of testing conditions.

4.2. Fracture-induced Biot coefficients

Pore-fluid loading is applied by injecting pressurized CO₂. The theoretical strain response to increments of fluid pressure in fractures p_c while keeping constant confining stresses and adsorption stress in the coal matrix (i.e., no variation of the sorbed amount n_r and of the thermodynamic pressure p_m of the fluid in the coal matrix) is derived from Equation (4).

$$\begin{cases} \left. \frac{\partial \varepsilon_r}{\partial p_c} \right|_{\sigma_a, \sigma_r, p_m} = \frac{1-\nu}{E} b_1 - \frac{\nu_3}{E_3} b_3 \\ \left. \frac{\partial \varepsilon_a}{\partial p_c} \right|_{\sigma_a, \sigma_r, p_m} = -\frac{2\nu_3}{E_3} b_1 + \frac{1}{E_3} b_3 \end{cases} \quad (6)$$

On the other hand, the stress response of the coal core to CO₂ injection at constant volume and constant adsorption stress conditions is equal to

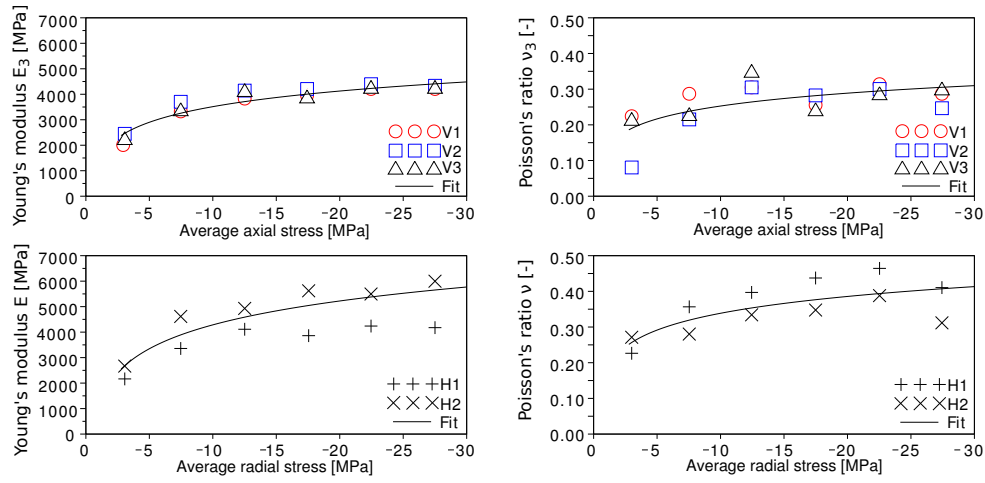


Figure 7: Summary of measured tangent elastic coefficients E , E_3 , ν , ν_3 as a function of axial and radial stress (drained moduli). Fitting functions (Elastic coefficient = $\text{cst}_1 + \text{cst}_2 \ln(-\text{Stress}/1\text{MPa})$) capture elastic nonlinearity. Coefficients (cst_1 , cst_2) are (1478 MPa, 884 MPa) for E_3 , (1172 MPa, 1352 MPa) for E , (0.133, 0.052) for ν_3 , and (0.182, 0.068) for ν .

$$\begin{cases} \left. \frac{\partial \sigma_r}{\partial p_c} \right|_{\varepsilon_a, \varepsilon_r, p_m} = -b_1 \\ \left. \frac{\partial \sigma_a}{\partial p_c} \right|_{\varepsilon_a, \varepsilon_r, p_m} = -b_3 \end{cases} \quad (7)$$

We will note, in particular, that the experimental determination of coefficients b_1 and b_3 is difficult because of the overlap of the kinetics of fluid transfer through the specimen fractures and fluid transfer from/to the coal matrix. These values will be estimated in the following section from the total response of coal cores to CO₂ injection including the adsorption response.

4.3. Adsorptive properties

The adsorptive properties of coal cores are tested with CO₂. CO₂ amount in bulk conditions is computed with Span and Wagner (1996) equation of state. Constant confining stresses are used to measure adsorptive parameters. Constant volume experiments will be used to validate the model predictions. Details follow.

4.3.1. Adsorption under constant confining stresses

In this type of experiments, a pump injects CO₂ at an objective constant CO₂ pressure (controlled by a pump upstream), while keeping constant total stress conditions (controlled by axial and radial stress manipulated by hydraulic servo controllers). Figure 8 shows an example of the time history response of coal core V1 to CO₂ injection (experiment C.S.V1 - Table 2). The experiment starts by increasing confining stresses to the level at which will be kept constant during the entire test ($\sigma_r = \sigma_a = -6$ MPa in this case – increase not seen in the figure). Then, CO₂ is injected into the specimen at the objective pressure. CO₂ enters the core from the bottom cap and exits

Table 2: Summary of results of CO₂ injection experiments performed at constant stress conditions.

Test type and specimen	Obj. CO ₂ pressure [MPa]	Total radial stress σ_r [MPa]	Total axial stress σ_a [MPa]	Total CO ₂ uptake n_T [mol/L]	Change of strain $\Delta\varepsilon$ \perp B.P. [-]	Change of strain $\Delta\varepsilon$ \parallel B.P. [-]
C.S.V1	5	-6	-6	1.73	+0.0077	+0.0061
C.S.V2a	10	-11	-12	2.83	+0.0086	-
C.S.V2b	10	-12	-12	2.95	+0.0082	+0.0102
C.S.V3	10	-12	-12	2.98	+0.0100	+0.0082
C.S.H1	5	-7	-7	1.42	-	+0.0058
C.S.H2	10	-11	-12	3.37	-	+0.0072

from the top loading cap. The pipe which exits from the top loading cap is closed with a needle valve, thus, there is a finite dummy volume in the downstream side of the specimen. The fluid pressures at loading caps are continuously measured and are named p_{US} for the pressure upstream and p_{DS} for the pressure downstream (See Figure 8-a). Additional data include axial and radial strains (Figure 8-b) and the amount of injected CO₂ measured from the upstream injection pump (Figure 8-c). The injected amount of CO₂ is corrected to subtract the amount which slowly diffuses through the nitrile membrane. This rate is well identified in experiment signatures and the value ranged from 0.015 to 0.045 mol/day depending on CO₂ pressure and radial effective stress. In adsorption experiments, the specimen is left about 6 days to equilibrate with CO₂. This period of time was sufficient to achieve steady-state conditions according to our strain measurements.

We identify two main regimes during CO₂ injection into the coal core

under constant confining stresses: (1) CO₂ enters fractures and macropores by advection as a function of core fracture permeability, and causes a poroelastic expansion due to decrease in effective stress, and (2) CO₂ reaches the coal matrix by advection and diffusion and adsorbs onto the coal matrix, which leads to adsorption-induced swelling (Figure 8-b,c). Both regimes promote core expansion (positive strain) and uptake of CO₂ (positive amount of injected CO₂). Fluid pressure upstream equilibrates with fluid pressure downstream in ~30 min in the experiment shown in Figure 8. The fluid pressure in fractures is expected to be the same everywhere at this point. Afterwards, adsorption-induced swelling prevails. The characteristic time t^* (set at $p_{DS} = 95\%p_{US}$ - based on Figure 8) helps establishing a rough estimate of the CO₂ uptaken and the swelling strain induced by each type of porosity (macropores and micropores).

Figure 9 shows the data from Figure 8 plotted independently of time. Plotting strains and the injected amount of CO₂ as a function of pressure (Figure 9-a,b) facilitates identifying the overlapping response of fluid filling the cleat pore space and fluid adsorbing on the coal matrix. The reference strains and injected amount of CO₂ measured at the time t^* when there is no more flow through the core are also plotted with point lines in Figure 9-a-d.

The data collected from Figures such as 8 and 9 let us measure the total change of strain caused by CO₂ injection and the total CO₂ delivery to the core assembly. The delivery of CO₂ to the piping system (upstream 3.9 cm³ and downstream 3.3 cm³) must be subtracted to estimate the net amount of total CO₂ uptake in the coal specimen. In the case of experiment C.S.V1, the coal total uptake is 0.1750 mol - 0.025 mol = 0.150 mol or 1.73

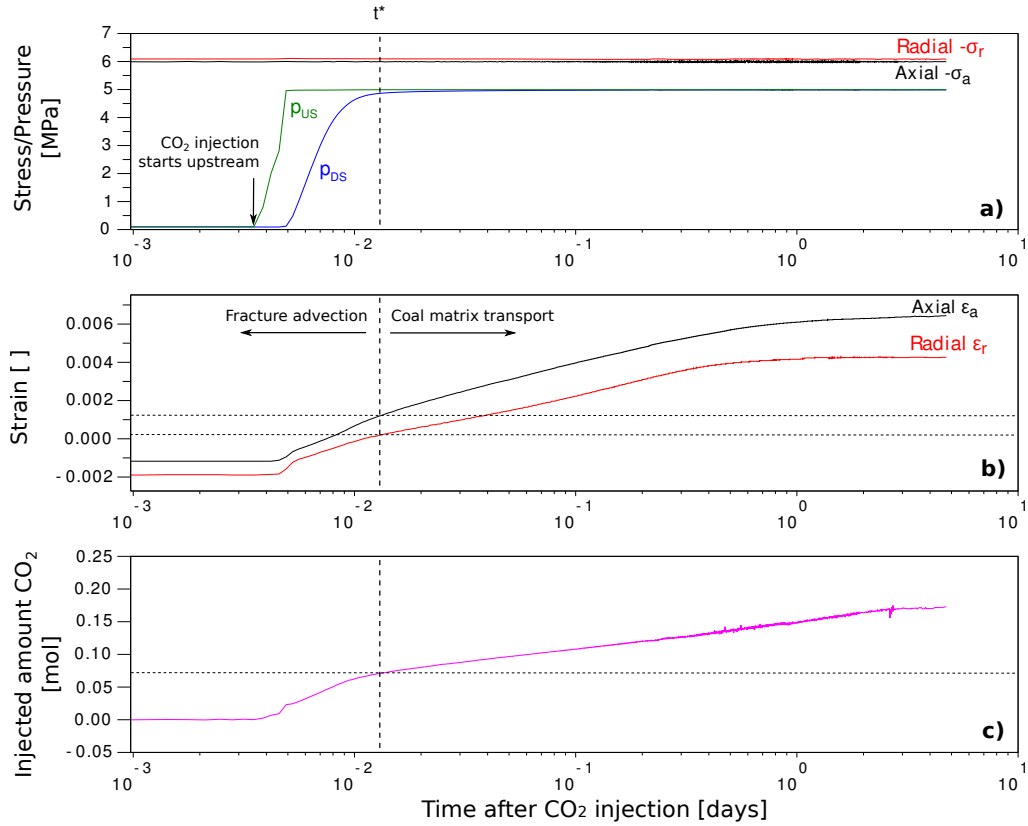


Figure 8: Time evolution of (a) fluid pressure, (b) strains, and (c) injected amount of CO₂ injection experiment C.S.V1 at constant confining stresses $\sigma_r = \sigma_a = -6$ MPa. The objective injection pressure is $p_{US} = p_{DS} = 5$ MPa. Temperature is 39.5°C.

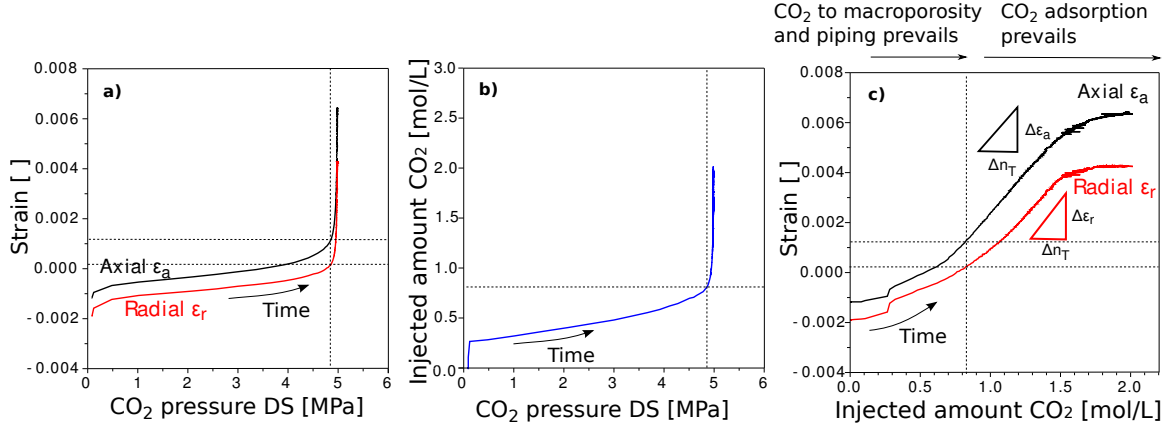


Figure 9: Response of specimen V1 (undeformed volume 86.8 cm^3 - experiment C.S.V1) to CO_2 injection at constant confining stresses (same data as in Figure 8). Measurements are plotted independently of time: (a) strain and CO_2 pressure downstream, (b) injected amount per unit volume and CO_2 pressure downstream, and (c) strain and injected amount per unit volume.

mol/L measured per unit volume, and the total change of strain after 5 days is $\varepsilon_a \sim +0.0077$ and $\varepsilon_r \sim +0.0061$ (includes poroelastic and adsorption-induced swelling). Let us introduce here an additional measurement which is a function only of the coupling between adsorption and strain: the ratio of change of strain to change of uptake amount per unit volume $\Delta\varepsilon_a/\Delta n_T$ and $\Delta\varepsilon_r/\Delta n_T$ at adsorption-dominated regimes. We compute these values as secant slopes of strain to total uptake after advection is over (after time t^*) and term them “swelling slopes”. For example, these quantities are $0.0043 \text{ (mol/L)}^{-1}$ and $0.0033 \text{ (mol/L)}^{-1}$, respectively for axial and radial strains in experiment C.S.V1 (Figure 9-c).

Table 2 shows a summary of experimental results for all CO_2 injection experiments performed keeping constant confining total stresses. Figure 10

plots the measured total uptake, total change of strains, and swelling slopes as a function of CO₂ pressure. All experiments show a consistent trend of declining differential swelling at incremental amount of adsorption (for example, at injected amounts of CO₂ greater than 1.5 mol/L in Figure 9-c). The discussion section explores further this phenomenon.

The total strain response upon injection (10-c) predicted by the poromechanical model results from the summation of strains caused by poroelastic effects in macropores (Equation 6) and the strain response to increments of adsorption stress s^a (a function of the thermodynamic pressure of the fluid phase in the coal matrix p_m), at constant confining radial σ_r and axial σ_a stresses and constant cleat fluid pressure p_c . This latter is equal to,

$$\begin{cases} \left. \frac{\partial \varepsilon_r}{\partial p_m} \right|_{\sigma_a, \sigma_r, p_c} = \left[\frac{1-\nu}{E} (1-b_1) - \frac{\nu_3}{E_3} (1-b_3) \right] \frac{ds^a}{dp_m} \\ \left. \frac{\partial \varepsilon_a}{\partial p_m} \right|_{\sigma_a, \sigma_r, p_c} = \left[-\frac{2\nu_3}{E_3} (1-b_1) + \frac{1}{E_3} (1-b_3) \right] \frac{ds^a}{dp_m} \end{cases} \quad (8)$$

The total uptake amount per unit volume (10-b) is obtained from Equation (3). The adsorption swelling slopes (10-d) are calculated from the full set of equations through numerical simulation.

The following sequence describes the process to determine the adsorptive-mechanical parameters of the coal core and coal matrix that fit best the experimental data according to the developed poromechanical model.

1. Estimation of core elastic moduli in dry conditions: We calculate the secant moduli from Figure (7) for a Terzaghi's effective stress that varies from 7.5 MPa to 1 MPa (approximate range for the set of experiments in Table 1). The corresponding values are $E = 2736$ MPa, $E_3 = 2551$ MPa, $\nu = 0.267$, $\nu_3 = 0.198$.

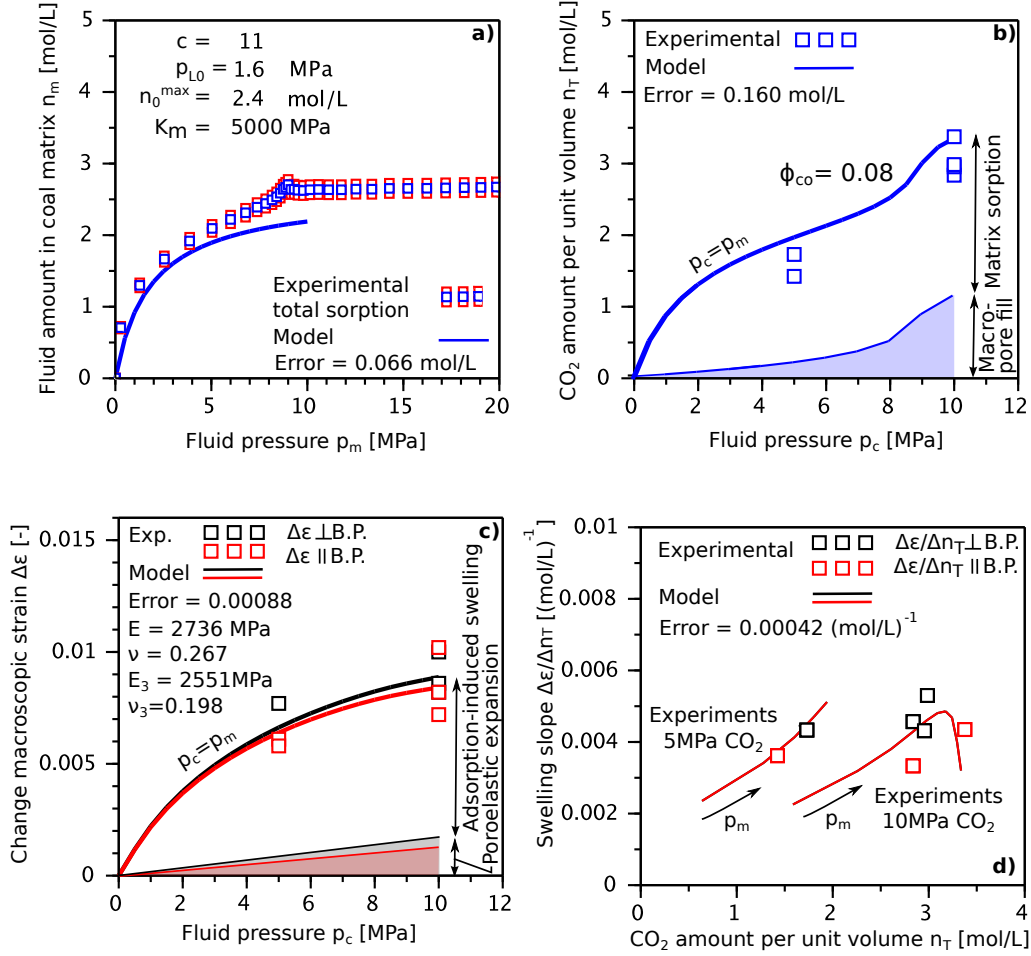


Figure 10: CO₂ uptake and adsorption-induced swelling in coal cores keeping constant confining stresses (See Table 2): experimental values and numerical simulation. Notice that total uptake amounts and change of strains are caused by macropore/fracture poroelastic response and micropore adsorptive response. (a) Coal matrix total sorption amount - from independent manometric tests (red squares indicate uncertainty - Auxiliary Material), (b) core total uptake amount of CO₂ per unit volume, (c) total change of core strains upon CO₂ injection, and (d) ratio of change of swelling strain to change of uptake amount during adsorption at constant pressure in fractures (Δp_c path not shown for model simulation).

2. Estimation of coal matrix bulk modulus K_m : We constrain K_m according to the bulk modulus of the coal core for the highest applied confining stress (~ 30 MPa), which varies between 4000 MPa and 4200 MPa. Hence, we adopt an upper bound $K_m = 5000$ MPa. Macro-Biot coefficients and modulus (b_1, b_3, N) are obtained from Equation (A.20).
3. Estimation of the initial macroporosity ϕ_{c0} : The total initial macroporosity varies from specimen to specimen. Considering that the Helium initial porosity of the set of coal cores varies from 11.2% to 14.4%, image analysis of X-ray slices yields a porosity of fractures (wider than $50 \mu\text{m}$) larger than 0.5 %, MPI yields a porosity about 1.5% of pores larger than $0.1 \mu\text{m}$, and the microporosity of coal matrix normally ranges from 3% to 10% (Gan et al., 1972; Lin et al., 1978), we set a mean macroporosity $\phi_{c0} = 8\%$ to invert a unique set of coal adsorption parameters. This porosity may seem too high for a coal core, but in this case it comprises pores up to the $0.1 \mu\text{m}$ scale.
4. Inversion of the parameters n_0^{max} , p_{L0} , and c ; where n_0^{max} and p_{L0} are parameters of the simplified adsorption isotherm at zero matrix strain $n_{m0}(p_m) = n_0^{max}[p_m/(p_{L0} + p_m)]$ and $c(p_m)$ is fixed to be pressure-independent as suggested by Espinoza et al. (2013). The inversion seeks to fit best (1) the coal matrix total sorption data n_m (these data is collected from an independent sorption experiment on crushed coal from the same coal seam - See Auxiliary Material), (2) the total uptake measured in the triaxial experiments n_T (Table 2), (3) the change of strains upon injection $\Delta\epsilon$ (parallel and perpendicular to the bedding plane - Table 2), and (4) the measured swelling slopes upon predominant ad-

Table 3: Best fitting measured and inverted model parameters. (Notes: *Indicates uncertainty. The shear modulus perpendicular to bedding C_{44} is not determined in this experimental study.

Core scale	Value		Matrix scale	Value	
E	2736 MPa	Measured	K_m	5000 MPa	Lower Bound
E_3	2551 MPa	Measured	n_0^{max}	2.4 mol/L	Inverted
ν	0.267	Measured	p_{L0}	1.6 MPa	Inverted
ν_3	0.198	Measured	c	11	Inverted
ϕ_0	0.08±0.02	Measured*			

sorption regime $\Delta\varepsilon/\Delta n_T$ (parallel and perpendicular to the bedding plane - Figure 10). The error is calculated with a two-norm criterion as a sum of the relative errors on the prediction of each amount.

The best fitting modeling results are shown in Figure 10. The best fitting parameters are summarized in Table 3. Calculated absolute errors are shown in Figure 10 as well.

Figure 10-b and 10-c show simulation results of total uptake n_T and total strain change $\Delta\varepsilon$ at equilibrium ($p_c = p_m$ at all times). Figures 10-b-c highlights the response expected from each porosity system. Figure 10-d shows the ratio of change of strain to change of total uptake after poroelastic expansion, i.e., change in fracture pressure occurs first (Δp_c) and adsorption-induced swelling follows (Δp_m). This type of simulation (increase of p_c first and p_m later) permits isolating the individual responses of the two porosity systems.

4.3.2. Adsorption under near constant volume conditions and model validation

The second testing procedure consists on constraining displacements upon CO₂ injection by imposing a near constant-volume condition. This stress path is obtained by periodic cancelation of swelling strains upon application of external total stresses. Figure 11 shows a time history example for experiment C.V.V1b performed at an average objective CO₂ injection pressure of 2 MPa (strictly, this experiment is performed with a pressure gradient for the sake of measuring permeability: $p_{US} = 2.5$ MPa and $p_{DS} = 1.5$ MPa). Results show that from an initial condition of total radial stress -3 MPa, axial total stress -10 MPa and no CO₂, CO₂ injection at near constant-volume conditions induced a change of radial and axial total stresses of -22 MPa in seven days. Figure 11 shows that the final change in total radial strain is -0.0001 and the change of axial strain is about $+0.0010$. This flow-through experiment does not allow a precise measurement of the specimen CO₂ uptake, hence, it is not reported.

Table 4 summarizes the result of two other similar experiments. The measured change of Terzaghi's effective stress ranges from 19 to 29 MPa. Experiment C.V.V1b was performed to confirm the results from C.V.V1a. Experiment C.V.V3 approached the upper stress limit of the triaxial cell, and hence, constant-volume condition could not be held after 5 hours of starting CO₂ injection. The specimen continued swelling $\Delta\varepsilon_a \sim +0.0007$ and $\Delta\varepsilon_r \sim +0.0014$ in 6 days at 36 MPa of hydrostatic confining stress. The fact that the specimen continued swelling indicates that higher confining stresses (>36 MPa) should have been applied to keep constant-volume condition. This was

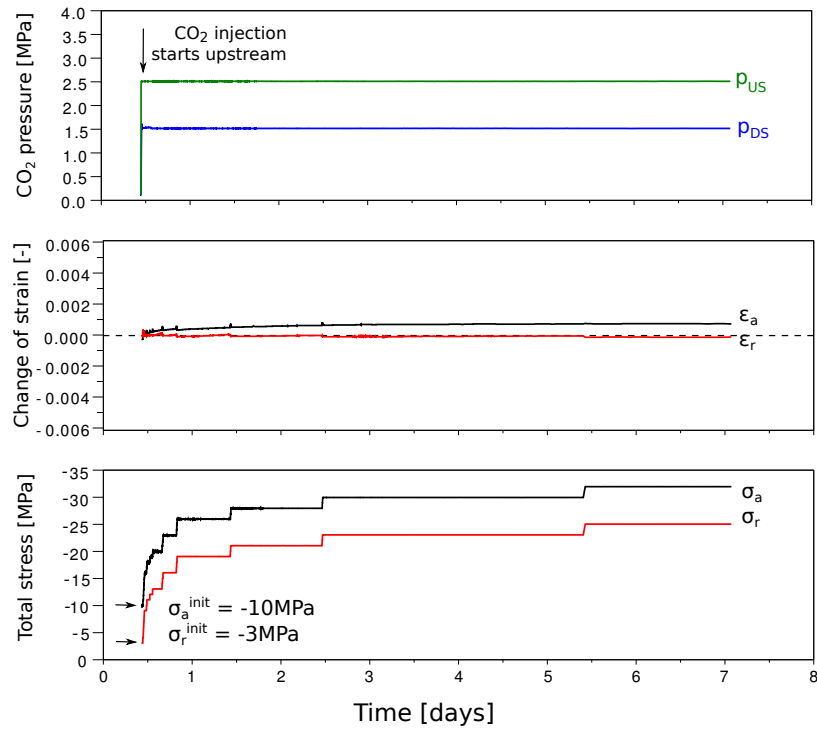


Figure 11: Time history of strains and total stresses upon CO₂ injection in core V1 keeping near constant volume conditions (Experiment C.V.V1b - Table 4).

Table 4: Summary of experimental results of CO₂ injection in cores performed at near constant volume conditions. (*Average pressure)

Test type and specimen	CO ₂ objective pressure [MPa]	Initial radial stress [MPa]	Initial axial stress [MPa]	Total CO ₂ uptake [mol/L]	Final radial stress [MPa]	Final axial stress [MPa]	Change in radial strain [-]	Change in axial strain [-]
C.V.V1a	2*	-3	-10	NA	-23	-30	-0.0005	-0.0002
C.V.V1b	2*	-3	-10	NA	-25	-32	-0.0001	+0.0010
C.V.V3	5	-2	-2	1.67	-36	-36	+0.0007	+0.0014

not a flow-through experiment, therefore it was possible to estimate the total uptake equal to 1.67 mol/L. It includes adsorption during swelling at 36 MPa. Less uptake amount would be expected in perfect isochoric conditions.

Let us now analyze the previous results in light of the double porosity poromechanical model and validate the parameters measured previously. Equation (7) shows that an injection of pore fluid under constant-volume condition ($\Delta\varepsilon_a = \Delta\varepsilon_r = 0$) results in an increase of compressive stress proportional to the macro Biot coefficients b_1 and b_3 . Since b_1 and b_3 are less than one, the increase in compressive stress should be at most equal to the change in fluid pressure. Yet, adsorption-induced stresses must be taken into account in the case of coal. The increase in total stress due to solely changes in adsorption stress (ds^a) can be obtained from Equation (3) and can be termed as a “macroscopic adsorption-induced stress” (macroscopic because weighed by $(1 - b_i)$). The rate of stress change respect to p_m is equal to

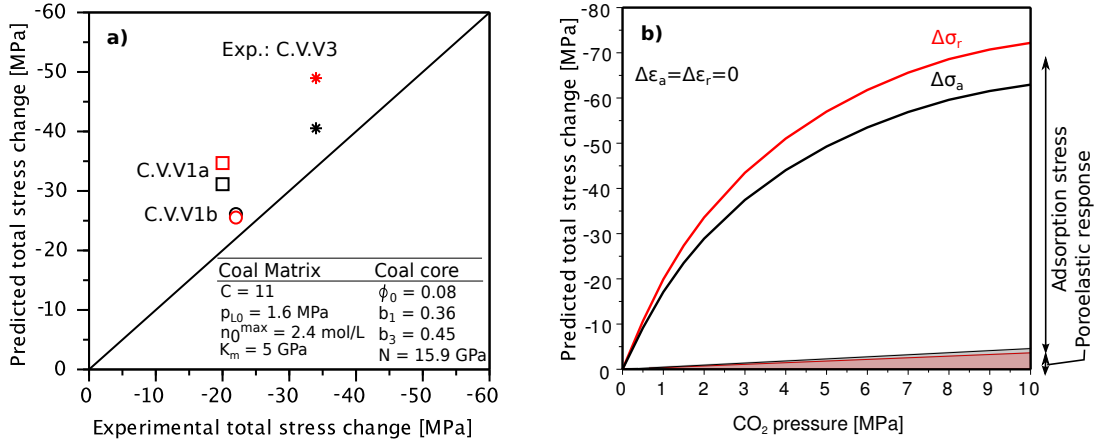


Figure 12: Change of total stress in coal cores induced by CO₂ injection at near constant-volume condition: (a) comparison between experimentally measured values and model predictions and (b) model-predicted change of stress at perfect constant-volume condition.

$$\begin{cases} \left. \frac{\partial \sigma_r}{\partial p_m} \right|_{\epsilon_a, \epsilon_r, p_c} = -(1 - b_1) \frac{ds^a}{dp_m} \\ \left. \frac{\partial \sigma_a}{\partial p_m} \right|_{\epsilon_a, \epsilon_r, p_c} = -(1 - b_3) \frac{ds^a}{dp_m} \end{cases} \quad (9)$$

Figure 12-a displays the experimentally measured changes in total stress upon CO₂ injection (mostly adsorption stresses) and the model predictions (Equation 3) based on the measurements of drained loading of dry coal specimens (secant moduli $E = 3998 \text{ MPa}$, $E_3 = 3396 \text{ MPa}$, $\nu = 0.333$, $\nu_3 = 0.248$ for a range of effective stress ~ 1 to 25 MPa), the estimated average macroporosity $\phi_{c0} = 0.08$, the lower bound for $K_m = 5000 \text{ MPa}$, and the inverted parameters ($n_{max}^0 = 2.4 \text{ mol/L}$, $p_{L0} = 1.6 \text{ MPa}$, $c = 11$) from swelling experiments at constant confining stress. The simulation results take into account that the sample was not strictly kept in isochoric conditions (i.e., includes experimental strains summarized in Table 4). All experimental values are between 3 to 16 MPa less compressive than the values predicted by the

1
2
3
4
5
6
7
8
9
10
11
12
13
14
15
16
17
18
19
20
21
22
23
24
25
26
27
28
29
30
31
32
33
34
35
36
37
38
39
40
41
42
43
44
45
46
47
48
49
50
51
52
53
54
55
56
57
58
59
60
61
62
63
64
65

model. The discussion section provides further insight into the mismatch of these results. Figure 12-b shows the change of stress predicted under perfect isochoric condition ($\varepsilon_a = \varepsilon_r = 0$) as a function of CO₂ pressure. The adsorption-induced stress is about 60 MPa at 10 MPa of CO₂ pressure.

4.4. Permeability measurements

We measured cleat permeability at constant flow rate regimes assuming Darcy compressible fluid flow (viscosity obtained from webbook.nist.gov). Fluid flow through cleats occurs at pressures higher than 1 MPa and mainly through micron-sized fractures. Therefore, Klinkenberg effect is disregarded.

4.4.1. Permeability of a CO₂-equilibrated core – Effect of effective stresses

We explored the permeability of specimen V1 to CO₂ in axial direction (on the plane of vertical fractures in the seam) varying radial and axial stresses at mean fracture fluid pressure of ~5.25 MPa, and pressure gradient of ~1.5 MPa over the length of the core. In order to cancel out the effect of adsorption stresses, the specimen is equilibrated with CO₂ for ~6 days at 5 MPa prior to permeability measurements, letting the coal matrix swell under constant confining stresses. Thereafter, a constant CO₂ gradient is imposed (upstream 6 MPa and downstream 4.5 MPa). The gradient is kept constant and relatively small to avoid changes in adsorption-induced stresses in time and in space throughout the specimen length. The effect of change of flow rate because of transient mechanically-induced desorption or sorption was neglected (this phenomenon is explained elsewhere (Hol et al., 2012)).

Figure 13 shows measured permeability as a function of radial and axial Terzaghi's effective stresses. The precision of permeability measurements

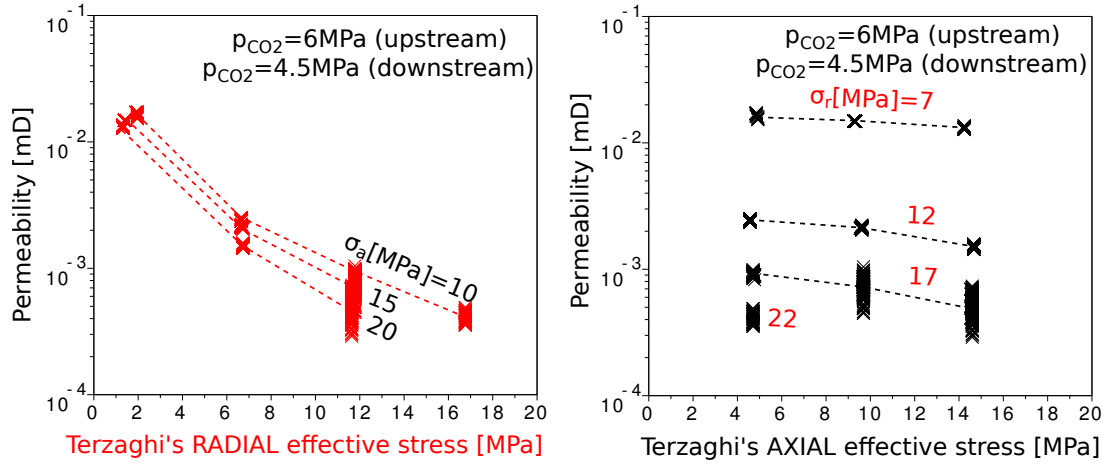


Figure 13: CO₂ permeability of specimen V1 subjected to various levels of effective stress in radial and axial directions. The dashed lines join data points at the same axial (left) or radial stress (right).

decreased with increasing effective stress, because the gradient of pressure was constant at all times. The value of fracture compressibility parameters which best fit Eq. (2) are $\alpha_r = -0.269 \text{ MPa}^{-1}$, $\alpha_a = -0.067 \text{ MPa}^{-1}$, and $k_0 = 0.033 \text{ mD}$ at zero Terzaghi's effective stress in radial and axial directions. The fitting is far from perfect but captures the main trend within the fitted interval (up to $\sigma'_r \sim 17 \text{ MPa}$ and $\sigma'_a \sim 15 \text{ MPa}$). The axial permeability of vertically cored specimens is about 4 times more sensitive to radial than to axial effective stresses. The measured stress sensitivity of permeability is within the range of values measured in the literature -0.23 to -0.46 MPa^{-1} (Somerton et al., 1975).

1
2
3
4
5
6
7
8
9
492 4.4.2. *Permeability evolution of a core during CO₂ adsorption at near con-*
10
11 *stant volume condition*
12

13 494 In order to resemble the conditions found in coal seams in-situ, we mea-
14
15 495 sured coal core permeability during the process of adsorption while keeping
16
17 496 near constant-volume condition. Constant-volume condition was chosen over
18
19 497 zero-lateral strain condition to avoid shearing the specimen. Figure 14 shows
20
21 498 the permeability measured during test C.V.V1b, for which the CO₂ pressure
22
23 499 was established upstream at $p_{US} = 2.5$ MPa and downstream at $p_{DS} = 1.5$
24
25 500 MPa (Figure 11-a). Permeability decreases more than two orders of magni-
26
27 501 tude from 0.02 mD to 0.0001mD as a result of increased Terzaghi's effective
28
29 502 stresses as a result of adsorption.

30 503 Let us now predict the variation of permeability for this experiment, based
31
32 504 on the previously measured stress-permeability relationship (parameters from
33
34 505 Figure 13) and the predicted induced adsorption stresses using the porome-
35
36 506 chanical model (Equation 3). Total stresses σ_a and σ_r can be calculated for
37
38 507 any equilibrium pressure or combination of p_c and p_m using Equation (3).
39
40 508 Thus, simply replacing the Terzaghi's effective stress $\sigma'_{ij} = -(\sigma_{ij} + p_c)$ in the
41
42 509 permeability Equation (2) allows us to calculate the permeability evolution
43
44 510 of the coal specimen upon adsorption. The results are plotted in Figure 14.
45
46 511 The predicted final effective radial and axial stress are about 27MPa and the
47
48 512 predicted permeability about 3 nD. In Figure (14), the solid line indicates
49
50 513 the predicted permeability in the range of stress-permeability fitted from ex-
51
52 514 perimental measurements (up to ~ 17 MPa radial effective stress) and the
53
54 515 dashed line shows the extrapolated permeability out of this fitting range.
55
56 516 The discussion section revisits the overestimation of permeability reduction.

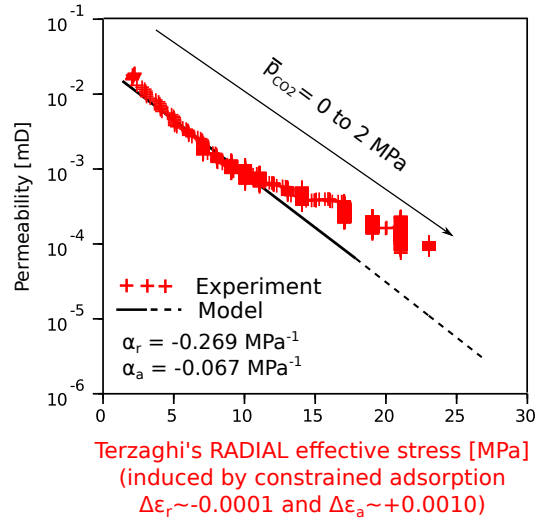


Figure 14: CO₂ permeability evolution of core V1b subjected to constrained adsorption under near constant-volume condition. The specimen develops stresses as a result of CO₂ injection and constrained swelling. Ensuing stresses lower measured permeability up to 100 times. Predicted permeability is calculated based on the change of effective stresses calculated with Equation (3) and permeability parameters from best fit of independent data in Figure (13). The dashed line indicates values of permeability extrapolated out from the experimental fitting range.

5. Discussion

5.1. Experimental testing

5.1.1. Specimen representativity

Measurements of rock properties from laboratory tests are usually biased by the length scale of specimens compared to the spatial variability and effective physical properties at reservoir scale. Major fractures such as master cleats cannot be sampled in specimen cores for triaxial testing. Hence, lower elastic moduli and higher permeability are expected at the seam scale than the values measured in core laboratory specimens.

An additional non-trivial feature affected by length scale is mechanical anisotropy. Coal laboratory tests in this article and in the literature (Day et al., 2010; Morcote et al., 2010; Espinoza et al., 2013) and shale (Wang, 2002) indicate that Young’s modulus in direction perpendicular to the bedding plane is lower than in direction parallel to the bedding plane $E_{\perp} < E_{\parallel}$, or equivalently that the Thomsen parameter $\epsilon^* = (C_{\parallel} - C_{\perp})/(2C_{\perp})$ is greater than zero (Thomsen, 1986). However, most master cleats are perpendicular to the bedding plane (Laubach et al., 1998). This fact suggests that there could be a mechanical anisotropy reversal such that at the seam scale $E_{\perp} > E_{\parallel}$.

Permeability measured in direction perpendicular to the bedding plane is expected to differ from the permeability in direction parallel to the bedding plane because of the tortuosity (spatial organization) of the cleat network and of the presence of interbedded low-permeability clay-rich layers. Scale issues are still present. In-situ measured seam permeability ranges from 0.1 to 100 mD (Scott et al., 2012), which is significantly higher than the

1
2
3
4
5
6
7
8
9
542 permeabilities we measured in the laboratory, which range from 0.0001 to 0.01
10
11 mD. Statistical analyses can help upscale laboratory measured permeability
12
13 (Lake and Srinivasan, 2004).
14

15
16 5.1.2. *Porous structure: a well defined double porosity system?*
17

18 Various experimental methods suggest the presence of a complex network
19
20 of pores that is far from being easily divided into two well defined porosity
21
22 systems. Naked-eye visual observation permits identifying fractures as large
23
24 as $\sim 500 \mu\text{m}$. X-ray tomography and SEM microscopy permit observing
25
26 smaller fractures in the range of $200 \mu\text{m}$ to $5 \mu\text{m}$. MIP and N_2 adsorp-
27
28 tion confirm the presence of small fractures, mesopores and micropores that
29
30 extend from $5 \mu\text{m}$ down to the nm scale (Figure 3).
31

32 For the sake of modeling and conceptualization, we have traced a line
33
34 dividing microporosity and macroporosity based on the predominant flow
35
36 regimes and poromechanical response. The simplified macroporosity system
37
38 is the one which is most conductive and has a negligible adsorption-induced
39
40 mechanical response. The simplified microporosity system is constituted by
41
42 pores that can uptake fluid at constant pressure in the macropore system and
43
44 whose solid part can develop a strong adsorption-induced response (strains
45
46 or stresses). Thus, the definition of macro and microporosity is based on the
47
48 conceptual ideas presented in Section 3, but may also depend on the length
49
50 scale of analysis.
51
52
53
54
55
56
57
58
59
60
61
62
63
64
65

1
2
3
4
5
6
7
8
9
10 563 5.1.3. *Experimental results: uncertainties, unexpected phenomena, and main*
11 564 *findings*
12

13 565 The measurement with the highest uncertainty is the total amount of up-
14
15 566 take because of diffusion of CO₂ through the confining membrane. During the
16
17 567 time length of experiments, the diffused amount could add up to an amount
18
19 568 as large as the effective total uptake amount. Fortunately, these “leaks” were
20
21 569 quite steady and measurable. Yet, the uncertainty is estimated to be as large
22
23 570 as 0.5 mol/L. A not-perfectly sealing but deformable membrane performed
24
25 571 better to measure mechanical properties than a tight but rigid membrane,
26
27 572 e.g., lead membrane. The uncertainty in determining total amount of uptake
28
29 573 impacts directly on the determination of the adsorption-strain coupling co-
30
31 574 efficient c , n_{max}^0 , and p_{L0} . We were able to reduce the uncertainty of these
32
33 575 inverted parameters by using additional sorption data on crushed coal from
34
35 576 the same coal seam (Figure 10-a).

36 577 We observed high elastic nonlinearity at low effective stress, as a result of
37
38 578 existing fractures. Nonlinearity lessened at high effective stress as fractures
39
40 579 closed. Using N₂ or He would have facilitated the measurement of porome-
41
42 580 chanical properties and macro Biot parameters (b_1, b_3), with less influence of
43
44 581 adsorption-induced response. Yet each fluid would yield its own “porome-
45
46 582 chanical signature” because each fluid has different affinity with coal surfaces
47
48 583 and can even access different pore sizes. Therefore, we preferred to test only
49
50 584 with CO₂.

51 585 The time required for CO₂ uptake and coal equilibration was based on the
52
53 586 measured specimen response through either strains or stresses. The allowed
54
55 587 equilibration time was enough to reach asymptotic trends in induced strains
56
57
58

1
2
3
4
5
6
7
8
9
10 588 or stresses suggesting that most of the sorption process had already hap-
11 589 pened. These measurements were adequate to measure the required model
12
13 590 parameters. Natural fractures facilitated relatively short equilibration times
14
15 591 from a few days to 10 days. Having a non-fractured core would have made
16
17 592 measurements much lengthier if not impossible in a practical time frame.

18
19 593 The change in swelling slope (Figure 9) in tests performed during adsorp-
20
21 594 tion at constant confining stress was a non-expected result. This reduction,
22
23 595 observed in other experiments as well, may be due to coal softening (reduc-
24
25 596 tion of elastic moduli), as observed previously in the literature (Czaplinski
26
27 597 and Holda, 1982; Masoudian et al., 2014) or CO₂-enhanced coal creep as
28
29 598 documented by Hagin and Zoback (2010) while adsorption-induced swelling
30
31 599 is still taking place.

32 600 Measured poroelastic and adsorption stresses have an uncertainty of ± 1
33
34 601 MPa. Controlling pressure pumps react with step changes of 1 MPa to
35
36 602 changes in strain of 10 μm , i.e., equivalent radial strain $\varepsilon \sim 5 \times 10^{-4}$. The
37
38 603 compressibility of the membrane is included in computing radial strains. The
39
40 604 corresponding uncertainty is less than 0.7 $\mu\text{m}/\text{MPa}$.

41 42 43 605 *5.2. Modeling*

44 45 606 *5.2.1. Main assumptions*

46
47 607 A sharp division between micro and macroporosity is not truly realistic (as
48
49 608 discussed in Section 6.1.2) but is useful for the sake of isolating predominant
50
51 609 phenomena at different length scales. Figures 10 and 12 help put in evidence
52
53 610 the response of each porosity system. The double porosity systems is well
54
55 611 suited for fluid flow simulation in media with heterogeneous permeability.

Both the coal matrix and the fractured coal may exhibit anisotropic properties (Pan and Connell, 2011). Non-fractured coal specimens and small cores generally develop anisotropy controlled by lamination planes $E_{\parallel} > E_{\perp}$ (Espinoza et al., 2013). Although it is possible to develop a model with anisotropy at both the coal matrix and fractured coal scales, in practical terms, it is convenient to group anisotropy at one of the two scales. Herein, we group anisotropy at the macro scale in views of analyzing mechanical anisotropy induced by master cleats at the fractured coal scale.

5.2.2. Parameter inversion

The most important parameters in defining the coupled response are the fractured coal elastic moduli C_{ij} , and coal matrix parameters n_0^{max} and $c(p_m)$, both of which define adsorption stress. Previous model validation studies for coal matrix specimens showed average coupling coefficient $c(p_m)$ for various coal specimens subjected to CH₄ or CO₂ swelling ranging from 5 to 10, with the highest values corresponding to CO₂ and the lowest ones to CH₄ (Brochard et al., 2012; Nikoosokhan et al., 2012; Espinoza et al., 2013). The adsorption-strain coupling coefficient is fixed pressure-independent $c(p_m) = c$ in this article as suggested by Espinoza et al. (2013). In fact rather than only c , the ratio c/K_m is found to be the one that permits fitting observed adsorption strains and stresses. The coal matrix bulk modulus K_m was fixed to a constant value in this article. Cleat porosity (macroporosity) varies for different samples and would vary also depending on the scale of analysis. Here we chose a constant value $\phi_c = 0.08$ in order to invert a unique set of parameters. Cleat porosity has a second-order importance in fitting induced strains (Figure 10-c) and does not play a role in fitting swelling slopes (Figure

10-d).

The determination of 10 independent parameters is challenging even in well controlled laboratory experiments, which limits the applicability of the full model to industry practice. However, the model remains as a powerful tool for investigating the effect of anisotropy in the permeability evolution of coal seams.

5.2.3. Model predictions

Implementing the fitted parameters in the model captures well various measurements including total uptake amount, induced strains/stresses and swelling slopes. The same parameters (except for elastic moduli) overestimate by 3 to 16 MPa the induced adsorption-induced stress when displacements are constrained upon adsorption. This overestimation may be due to heterogeneity of coal from sample to sample and measured elastic moduli, an inaccurate estimation of secant elastic moduli, or also to the fact that coal may soften with significant amounts of sorbed CO₂ with concomitant reduction of induced stresses. Creep may also play a role in canceling the swelling strains as discussed before.

The overestimation in reduction of permeability (Figure 14) stems from adopting a linear log(permeability)–stress law. Predictions are good in the interval at which the permeability is fitted from experimental data, but extrapolations deviate beyond the fitting range. More complex models can capture a “hard permeability” which makes permeability plateau at high effective stress, and thus capture the nonlinear dependence of the logarithm of permeability as a function of effective stress (Liu and Rutqvist, 2010). A simple logarithmic correlation based on Terzaghi’s effective stress seems to

be appropriate over a defined stress range. Yet, coal seams subjected to CH₄ depletion and/or CO₂ injection under in-situ conditions may experience significant shear stresses which promotes fracture slip and dilation and coal fines production with a significant impact on seam permeability as well (Palmer, 2008; Okotie and Moore, 2010).

5.3. Implications on coal bed methane production and CO₂ geological storage

Our stress-based coupled model offers new insights into the prediction of natural gas recovery and injectivity during CO₂ injection in unmineable coal seams. The model can predict order of magnitude changes in permeability applying the appropriate boundary conditions.

We have measured significant changes of stress associated with sorption under constrained condition, termed as adsorption-induced stresses. Conversely, desorption is expected to cause stress relaxation. If boundary conditions are close to oedometric (constant vertical stress and zero lateral strain), then a significant decrease in horizontal stress at constant vertical stress would be expected upon desorption with ensuing increase of stress anisotropy that could lead to shear failure and fines production (Okotie and Moore, 2010).

6. Conclusions

Meaningful coal testing is challenging because of the difficulties in obtaining representative fractured coal cores, separating the competing fracture advection and matrix adsorption phenomena, and reproducing reservoir in-situ conditions during testing in the laboratory.

1
2
3
4
5
6
7
8
9
10
11
12
13
14
15
16
17
18
19
20
21
22
23
24
25
26
27
28
29
30
31
32
33
34
35
36
37
38
39
40
41
42
43
44
45
46
47
48
49
50
51
52
53
54
55
56
57
58
59
60
61
62
63
64
65

685 We performed tests on moderately fractured sub-bituminous/bituminous
686 coal cores and used CO₂ as a proxy for CH₄. Experimental results from
687 triaxial testing show that (1) fractured coal has a significant non-linear elastic
688 behavior, (2) fractured coal cores show mechanical anisotropy, (3) swelling
689 strains, swelling stresses and total uptake are affected by the response of the
690 macroporous and microporous systems, and (4) permeability is four times
691 more sensitive to radial (lateral) stress than to axial (vertical) stress. Overall,
692 experimental results highlight the difference between the two porous systems
693 through their poromechanical response. Experiments under near constant
694 volume condition show that effective stresses increase significantly during
695 adsorption. The increase in effective stress is the main driver for changing
696 core permeability. The measured changes of effective stress was as high as
697 +29 MPa for CO₂ injection at 5 MPa of pressure.

698 We developed a double porosity poromechanical model to capture the
699 adsorptive-mechanical response of transverse isotropic fractured coal. The
700 adsorptive-mechanical coupling is modeled through an adsorption stress func-
701 tion which depends on the coal matrix properties. The model is fully cou-
702 pled, therefore, it permits quantifying the influence of adsorption on strain
703 and stresses as well as the influence of stresses and strains on adsorption.
704 The discrimination of two porosity levels permits isolating poromechanical
705 responses and calculating fluid amounts from either fractures or the coal
706 matrix. Permeability is calculated as function Terzaghi's effective stress.

707 The developed double porosity model let us recognize the key porome-
708 chanical properties at each scale and measure relevant parameters. Core
709 scale measurements and CO₂ injection experimental data matching let us

1
2
3
4
5
6
7
8
9
10 recover the mechanical-adsorptive properties of the coal matrix such as bulk
11 modulus, isochoric adsorption isotherm, and the adsorption-strain coupling
12 coefficient. The model predicts significant adsorption-induced stresses and
13 order-of-magnitude changes in permeability as measured experimentally.
14
15
16
17

18 **Acknowledgements**

19
20

21 This work was supported by Total S.A. The technical support provided
22
23 by E. De Laure and his team at Laboratoire Navier-CERMES is greatly
24 appreciated. We are thankful to N. Lenoir who performed the X-ray imaging,
25
26 to H. Daigle who provided the N₂ adsorption results, and to the anonymous
27
28 reviewers who helped improving this article.
29
30
31
32
33
34
35
36
37
38
39
40
41
42
43
44
45
46
47
48
49
50
51
52
53
54
55
56
57
58
59
60
61
62
63
64
65

7. Symbols

α	Fracture compressibility coefficient for permeability law [MPa ⁻¹]
ϵ_m	Volumetric strain of the coal matrix [-]
ε_{ij}	Strain tensor defined at the fractured coal scale [-]
ϕ_c	Cleat porosity or macroporosity [-]
μ	Chemical potential [J/mol]
ν, ν_3	Poisson's ratio parallel and perpendicular to bedding [-]
σ_{ij}	Total stress tensor defined at the fractured coal scale [Pa]
σ'_{ij}	Terzaghi's effective stress tensor defined at the fractured coal scale [Pa]
ρ_b	Bulk molar density of the fluid [mol/L]
b_1, b_3	Biot coefficient parallel and perpendicular to bedding [-]
c	Adsorption-strain coupling coefficient [-]
k	Permeability [darcy]
k_0	Reference permeability at zero effective stress [darcy]
n_m	Fluid amount in the coal matrix per unit volume of coal matrix [mol/L]
n_0^{max}	Asymptotic parameter of constant matrix volume Langmuir isotherm [mol/L]
n_r	Fluid amount in the coal matrix per unit volume of fractured coal [mol/L]
n_T	Total fluid amount per unit volume of fractured coal REV [mol/L]
p_c	Pressure of fluid in cleats [Pa]
p_m	Thermodynamical pressure of fluid in the coal matrix [Pa]
p_{L0}	Langmuir pressure of constant matrix volume Langmuir isotherm [Pa]
s^a	Coal matrix adsorption stress [Pa]
C_{ij}	fractured coal stiffness tensor coefficient [Pa]
E, E_3	Young's modulus parallel and perpendicular to bedding [Pa]
K_m	Bulk modulus of the coal matrix [Pa]
\bar{V}_b	Molar volume of the fluid in bulk conditions [L/mol]

Appendix A. Model derivation

The model derivation extends the model developed by Nikoosokhan et al. (2012, 2014) to consider transverse isotropy. The model is based on energy conservation and follows from a thermodynamical formulation.

Appendix A.1. Energy balance equation

Consider a representative elementary volume (REV) of fractured coal (Figure 1). Let us denote the Helmholtz free energy of the solid coal matrix (including the energy of fluid in micropores) per unit volume of undeformed fractured coal as f_m [J/L]. Energy can be added to this system by strain work of the stress tensor $\sigma_{ij}d\varepsilon_{ij}$, by strain work of cleat pressure on fracture walls $p_c d\phi_c$, or by adding fluid to the micropores in the coal matrix μdn_r . Energy conservation under isothermal conditions yields

$$df_m = \sum_{i,j} \sigma_{ij} d\varepsilon_{ij} + p_c d\phi_c + \mu dn_r \quad (\text{A.1})$$

being σ_{ij} the total stress tensor acting on a REV of fractured coal (i.e., coal matrix and cleats) [Pa], ε_{ij} the strain tensor of a REV of fractured coal [-], p_c the fluid pressure in cleats [Pa], ϕ_c the Lagrangian porosity of cleats within the REV [-] (calculated respect to the original undeformed reference volume of REV), μ the molar chemical potential of adsorbed fluid in the coal matrix [J/mol], and n_r the number of adsorbed moles in the coal matrix per unit volume of REV of undeformed fractured coal (includes fractures volume) [mol/L]. A Legendre transform lets us change variables, so that the following holds:

$$d(f_m - n_r \mu) = \sum_{i,j} \sigma_{ij} d\varepsilon_{ij} + p_c d\phi_c - n_r d\mu \quad (\text{A.2})$$

The development of the model consists in finding expressions to the variables σ_{ij} , p_c , and n_r as a function of the state variables ε_{ij} , ϕ_c , and μ . This formulation differs from the one by Espinoza et al. (2013) because it includes explicitly a well defined fracture porosity and the effect of fracture compressibility. Moreover, in this formulation stresses and strains are defined at the scale of fractured coal rather than at the scale of the coal matrix.

Appendix A.2. Constitutive equations

Appendix A.2.1. Total amount of fluid in the coal matrix per unit of volume of fractured coal

Rather than defining a microporosity of the coal matrix, let us define n_m [mol/L] as the total amount of fluid in the coal matrix per unit volume of undeformed coal matrix (it does not include fracture volume). The undeformed coal matrix volume is chosen as a reference volume, so that the sorption per unit mass [mol/g] can be obtained knowing the reference bulk mass density. As suggested by Brochard et al. (2012), the amount of fluid within the coal matrix depends on the fluid chemical potential μ (or pressure) and coal matrix volumetric strain ϵ_m . Furthermore, Brochard et al. (2012) show that the total amount of fluid in a piece of isotropic coal matrix can be well approximated by a first-order expansion of the total amount of fluid in the coal matrix with respect to the coal matrix volumetric strain ϵ_m , thus

$$n_m(p_m, \epsilon_m) = n_{m0}(p_m) [1 + c(p_m) \epsilon_m] \quad (\text{A.3})$$

where $n_{m0}(p_m)$ is the adsorption isotherm at zero strain, $c(p_m)$ is a coefficient which quantifies the effect of strain on adsorption capacity, and p_m is the pressure of the bulk fluid at the same chemical potential μ as the adsorbed phase in the coal matrix, termed “thermodynamic pressure”. The coupling coefficient $c(p_m)$ is positive for fluids that make coal swell. This simple linear expansion permits accounting for effects such as swelling strain, adsorption stress, and mechanically induced desorption.

In order to add up fluid amounts more easily, let us define n_r the amount of fluid within the coal matrix per unit volume of REV of undeformed fractured coal, which in terms of the amount of fluid within the coal matrix n_m per unit volume of undeformed coal matrix and reference cleat porosity ϕ_{c0} results as

$$n_r(p_m, \varepsilon_{ij}, \phi_c) = (1 - \phi_{c0})n_m(p_m, \epsilon_m) \quad (\text{A.4})$$

The volumetric strain at the fractured coal REV scale $\epsilon = \varepsilon_{11} + \varepsilon_{22} + \varepsilon_{33}$ is related to the coal matrix volumetric strain ϵ_m in an exact manner through the following relation (Coussy, 2010):

$$\epsilon_m = \frac{\epsilon - (\phi_c - \phi_{c0})}{1 - \phi_{c0}} \quad (\text{A.5})$$

where ϕ_{c0} is the reference porosity of the undeformed fractured coal.

Appendix A.2.2. Stress-adsorption relationship

By applying Maxwell’s relations on Eq. (A.2) and taking partial cross derivatives respect to ε_{ij} and μ we obtain

$$\left. \frac{\partial^2(f_m - n_r\mu)}{\partial \varepsilon_{ij} \partial \mu} \right|_{\phi_c} = \left. \frac{\partial^2(f_m - n_r\mu)}{\partial \mu \partial \varepsilon_{ij}} \right|_{\phi_c} \quad (\text{A.6})$$

So that integration leads to,

$$\left. \frac{\partial \sigma_{ij}}{\partial \mu} \right|_{\phi_c, \varepsilon_{kl} \neq ij} = - \left. \frac{\partial n_r}{\partial \varepsilon_{ij}} \right|_{\phi_c, \mu, \varepsilon_{kl} \neq ij} \quad (\text{A.7})$$

Let us write $\partial \varepsilon_{ij}$ in terms of ϵ_m and ϕ_{c0} and ∂n_r in terms of n_m using Eq. (A.4) and (A.5). This replacement leads to the following equation,

$$\begin{cases} - \left. \frac{\partial n_r}{\partial \varepsilon_{ij}} \right|_{\phi_c, \mu} = - \frac{(1-\phi_{c0})}{(1-\phi_{c0})} \left. \frac{\partial n_m}{\partial \epsilon_m} \right|_{\mu} = - \left. \frac{\partial n_m}{\partial \epsilon_m} \right|_{\mu} & \text{if } i = j \\ - \left. \frac{\partial n_r}{\partial \varepsilon_{ij}} \right|_{\phi_c, \mu} = 0 & \text{if } i \neq j \end{cases} \quad (\text{A.8})$$

By integrating Eq. (A.7) on the molar chemical potential μ and replacing the right hand side with Eq. (A.8), we obtain

$$\sigma_{ij} = \Psi_{ij}(\underline{\varepsilon}, \phi_c) - \int_{-\infty}^{\mu} \left. \frac{\partial n_m}{\partial \epsilon_m} \right|_{\mu} d\mu \delta_{ij} \quad (\text{A.9})$$

Gibbs-Duhem equation lets us express the variation in chemical potential as a function of the thermodynamical pressure as $d\mu = \bar{V}_b(p_m) dp_m$ for isothermal conditions, where \bar{V}_b is the molar volume of the fluid in bulk conditions as a function of temperature and pressure, therefore we can write,

$$\sigma_{ij} = \Psi_{ij}(\underline{\varepsilon}, \phi_c) - \int_0^{p_m} \left. \frac{\partial n_m}{\partial \epsilon_m} \right|_p \bar{V}_b(p_m) dp_m \delta_{ij} \quad (\text{A.10})$$

The first term to the right of the equality Ψ_{ij} represents the poroelastic response of the fractured coal to bulk strains and fracture pressure (without accounting for adsorption phenomena) and the integral term represents the response of the coal matrix to fluid adsorption as a function of fluid pressure and coal matrix strain. The integral term quantifies the stress needed to keep the coal matrix at zero volumetric strain during adsorption, and is termed

“adsorption stress” s^a as motivated by analogy with the theory formulated by Ravikovitch and Neimark (2006), i.e.,

$$s^a(p_m) = \int_0^{p_m} \frac{\partial n_m}{\partial \epsilon_m} \bigg|_p \bar{V}_b(p_m) dp_m \quad (\text{A.11})$$

Equation A.10 written in terms of $s^a(p_m)$ is

$$\sigma_{ij} = \Psi_{ij}(\underline{\epsilon}, \phi_c) - s^a(p_m) \delta_{ij} \quad (\text{A.12})$$

In fact, the integrand of $s^a(p_m)$ can be viewed as a pressure-dependent Biot-like coefficient b^* [-], (in the sense that $b^* = d\sigma/dp|_\epsilon$), which according to Eq. (A.3) expands to,

$$b^*(p_m) = \frac{\partial n_m}{\partial \epsilon_m} \bigg|_p \bar{V}_b(p_m) = c(p_m) n_{m0}(p_m) \bar{V}_b(p_m) \quad (\text{A.13})$$

Appendix A.2.3. Pressure-adsorption relationship

By applying Maxwell’s relations on Eq. (A.2) and taking cross partial derivatives with respect to ϕ_c and μ the following holds

$$\frac{\partial^2(f_m - n_r \mu)}{\partial \phi_c \partial \mu} \bigg|_{\epsilon_{ij}} = \frac{\partial^2(f_m - n_r \mu)}{\partial \mu \partial \phi_c} \bigg|_{\epsilon_{ij}} \quad (\text{A.14})$$

so that,

$$\frac{\partial p_c}{\partial \mu} \bigg|_{\epsilon_{ij}, \phi_c} = - \frac{\partial n_r}{\partial \phi_c} \bigg|_{\epsilon_{ij}, \mu} \quad (\text{A.15})$$

By using the micromechanical Eq. (A.5), the latter equation is equivalent to

$$\frac{\partial p_c}{\partial \mu} \bigg|_{\epsilon_{ij}, \phi_c} = \frac{\partial n_m}{\partial \epsilon_m} \bigg|_\mu \quad (\text{A.16})$$

Integration of this latter equation on the molar chemical potential μ leads
to

$$p_c = \Psi'_{ij}(\underline{\underline{\epsilon}}, \phi_c) + \int_{-\infty}^{\mu} \frac{\partial n_m}{\partial \epsilon_m} \Big|_{\mu} d\mu \quad (\text{A.17})$$

Using Gibbs-Duhem equation as before and recalling the definition of
adsorption stress we obtain,

$$p_c = \Psi'_{ij}(\underline{\underline{\epsilon}}, \phi_c) + s^a(p_m) \quad (\text{A.18})$$

The function Ψ'_{ij} represents the poroelastic response of the fractured coal
to bulk strains and changes in porosity (without accounting for adsorption
phenomena).

Appendix A.3. Transverse isotropic poroelasticity - Final equations

Let us approximate the behavior of fractured coal assuming transverse
isotropy around the axis perpendicular to the bedding plane, from now on
assigned to axis number 3. The functions Ψ_{ij} and Ψ'_{ij} for linear elastic trans-
verse isotropic poroelastic solids with principal directions of the Biot tensor
coinciding with the axes of symmetry of the fractured coal are summarized
in the following set of equations Coussy (2004),

$$\left\{ \begin{array}{lcl} \sigma_{11}(\underline{\underline{\varepsilon}}, \phi_c - \phi_{c0}) & = & C_{11}\varepsilon_{11} + C_{12}\varepsilon_{22} + C_{13}\varepsilon_{33} - b_1 N [(\phi_c - \phi_{c0}) - b_1(\varepsilon_{11} + \varepsilon_{22}) - b_3\varepsilon_{33}] \\ \sigma_{22}(\underline{\underline{\varepsilon}}, \phi_c - \phi_{c0}) & = & C_{12}\varepsilon_{11} + C_{11}\varepsilon_{22} + C_{13}\varepsilon_{33} - b_1 N [(\phi_c - \phi_{c0}) - b_1(\varepsilon_{11} + \varepsilon_{22}) - b_3\varepsilon_{33}] \\ \sigma_{33}(\underline{\underline{\varepsilon}}, \phi_c - \phi_{c0}) & = & C_{13}\varepsilon_{11} + C_{13}\varepsilon_{22} + C_{33}\varepsilon_{33} - b_3 N [(\phi_c - \phi_{c0}) - b_1(\varepsilon_{11} + \varepsilon_{22}) - b_3\varepsilon_{33}] \\ \sigma_{23}(\underline{\underline{\varepsilon}}, \phi_c - \phi_{c0}) & = & 2C_{44}\varepsilon_{23} \\ \sigma_{31}(\underline{\underline{\varepsilon}}, \phi_c - \phi_{c0}) & = & 2C_{44}\varepsilon_{31} \\ \sigma_{12}(\underline{\underline{\varepsilon}}, \phi_c - \phi_{c0}) & = & 2\frac{C_{11}-C_{12}}{2}\varepsilon_{12} \\ p_c(\underline{\underline{\varepsilon}}, \phi_c - \phi_{c0}) & = & N [(\phi_c - \phi_{c0}) - b_1(\varepsilon_{11} + \varepsilon_{22}) - b_3\varepsilon_{33}] \end{array} \right. \quad (\text{A.19})$$

where C_{ij} are elastic coefficients of the stiffness tensor. The macro-poromechanical parameters (b_1, b_3, N) relate to the coal matrix bulk modulus K_m as follows,

$$\left\{ \begin{array}{lcl} b_1 & = & 1 - \frac{(C_{11}+C_{12}+C_{13})/3}{K_m} \\ b_3 & = & 1 - \frac{(2C_{13}+C_{33})/3}{K_m} \\ \frac{1}{N} & = & \frac{(2b_1+b_3)/3-\phi_{c0}}{K_m} \end{array} \right. \quad (\text{A.20})$$

The poromechanical parameters capture the effect of pore/fracture compressibility on the bulk fractured coal elastic moduli. These equations are valid for any transverse isotropic porous solid with a well defined porosity ϕ_c . The last step consists in plugging the macro-poromechanical equations of the fractured coal (Eq. A.19) in the general equations of the stress tensor σ_{ij} (Eq. A.12) and pressure of fluids in cleats p_c (Eq. A.18) developed to consider matrix adsorption and swelling. Hence, the final set of equations results in Equation 1 in Section 2.

References

- Brochard, L., Vandamme, M., Pellenq, R.J.M., 2012. Poromechanics of microporous media. *Journal of the Mechanics and Physics of Solids* 60, 606–622.
- Ceglarska-Stefanska, G., Czaplinski, A., 1993. Correlation between sorption and dilatometric processes in hard coals. *Fuel* 72, 413–417.
- Ceglarska-Stefanska, G., Zarebska, K., 2002. The competitive sorption of CO₂ and CH₄ with regard to the release of methane from coal. *Fuel Processing Technology* 77-78, 423–429.
- Cheng, A.D., 1997. Material coefficients of anisotropic poroelasticity. *International Journal of Rock Mechanics and Mining Sciences* 34, 199–205.
- Chikatamarla, L., Cui, X., Bustin, R., 2004. Implications of volumetric swelling/shrinkage of coal in sequestration of acid gases, in: *International Coalbed Methane Symposium - Tuscaloosa, Alabama*.
- Cody, G.D., Larsen, J.W., Siskin, M., 1988. Anisotropic solvent swelling of coals. *Energy & Fuels* 2, 340–344. doi:10.1021/ef00009a020.
- Connell, L.D., Lu, M., Pan, Z., 2010. An analytical coal permeability model for tri-axial strain and stress conditions. *International Journal of Coal Geology* 84, 103–114. doi:10.1016/j.coal.2010.08.011.
- Coussy, O., 2004. *Poromechanics*. Wiley.
- Coussy, O., 2010. *Mechanics and Physics of Porous Solids*. Wiley.

- 1
- 2
- 3
- 4
- 5
- 6
- 7
- 8
- 9
- 10 853 Cowin, S.C., 2004. Anisotropic poroelasticity: fabric tensor formulation.
- 11 854 Mechanics of Materials 36, 665–677. doi:10.1016/j.mechmat.2003.05.001.
- 12
- 13
- 14 855 Cui, X., Bustin, R.M., Chikatamarla, L., 2007. Adsorption-induced coal
- 15 swelling and stress: Implications for methane production and acid gas
- 16 856 sequestration into coal seams. Journal of Geophysical Research 112.
- 17 857 doi:10.1029/2004JB003482.
- 18 858
- 19
- 20
- 21
- 22 859 Czaplinski, A., Holda, S., 1982. Changes in mechanical properties of coal
- 23 due to sorption of carbon dioxide vapour. Fuel 61, 1281–1282.
- 24 860
- 25
- 26
- 27 861 Day, S., Fry, R., Sakurovs, R., 2008. Swelling of Australian coals in
- 28 supercritical CO₂. International Journal of Coal Geology 74, 41–52.
- 29 862 doi:10.1016/j.coal.2007.09.006.
- 30 863
- 31
- 32
- 33 864 Day, S., Fry, R., Sakurovs, R., Weir, S., 2010. Swelling of coals by supercrit-
- 35 865 ical gases and its relationship to sorption. Energy & Fuels 24, 2777–2783.
- 36 866 doi:10.1021/ef901588h.
- 37
- 38
- 39
- 40 867 EIA, 2013. International Energy Outlook 2013 - Report number: DOE/EIA-
- 41 0484(2013). Technical Report.
- 42 868
- 43
- 44
- 45 869 Espinoza, D.N., Vandamme, M., Dangla, P., Pereira, J.M., Vidal-Gilbert, S.,
- 46 2013. A transverse isotropic model for microporous solids - Application
- 47 870 to coal matrix adsorption and swelling. Journal of Geophysical Research -
- 48 Solid Earth 118, 6113–6123.
- 49 871
- 50 872
- 51
- 52
- 53 873 Gale, J., 2004. Geological storage of CO₂: What do we know, where are the
- 54 gaps and what more needs to be done? Energy 29, 1329–1338.
- 55 874
- 56
- 57
- 58
- 59
- 60
- 61
- 62
- 63
- 64
- 65

- 1
- 2
- 3
- 4
- 5
- 6
- 7
- 8
- 9
- 10 875 Gan, H., Nandi, S., Walker, P., 1972. Nature of the porosity in American
- 11 876 coals. *Fuel* 51, 272–277. doi:10.1016/0016-2361(72)90003-8.
- 12
- 13
- 14 877 Hagin, P., Zoback, M.D., 2010. Laboratory studies of the compressibility
- 15 878 and permeability of low-rank coal samples from the Powder River Basin,
- 16 879 Wyoming, USA, in: ARMA 10-170.
- 17
- 18
- 19
- 20 880 Hol, S., Peach, C.J., Spiers, C.J., 2012. Effect of 3-D stress state on ad-
- 21 881 sorption of CO₂ by coal. *International Journal of Coal Geology* 93, 1–15.
- 22 882 doi:10.1016/j.coal.2012.01.001.
- 23
- 24
- 25
- 26 883 Hol, S., Spiers, C.J., 2012. Competition between adsorption-induced
- 27 884 swelling and elastic compression of coal at CO₂ pressures up to
- 28 885 100MPa. *Journal of the Mechanics and Physics of Solids* 60, 1862–1882.
- 29 886 doi:10.1016/j.jmps.2012.06.012.
- 30
- 31
- 32
- 33
- 34
- 35 887 Hu, D., Zhou, H., Zhang, F., Shao, J., 2010. Evolution of poroe-
- 36 888 lastic properties and permeability in damaged sandstone. *Interna-*
- 37 889 *tional Journal of Rock Mechanics and Mining Sciences* 47, 962–973.
- 38 890 doi:10.1016/j.ijrmms.2010.06.007.
- 39
- 40
- 41
- 42
- 43 891 IEA, 2013. Key world energy statistics 2013. Technical Report.
- 44
- 45
- 46 892 Lake, L.W., Srinivasan, S., 2004. Statistical scale-up of reservoir properties:
- 47 893 concepts and applications. *Journal of Petroleum Science and Engineering*
- 48 894 44, 27–39. doi:10.1016/j.petrol.2004.02.003.
- 49
- 50
- 51
- 52 895 Laubach, S.E., Marrett, R.A., Olson, J.E., Scott, A.R., 1998. Characteristics
- 53 896 and origins of coal cleat: A review. *International Journal of Coal Geology*
- 54 897 35, 175–207.
- 55
- 56
- 57
- 58
- 59
- 60
- 61
- 62
- 63
- 64
- 65

- 1
2
3
4
5
6
7
8
9
898 Levine, J.R., 1996. Model study of the influence of matrix shrinkage on
10 absolute permeability of coal bed reservoirs. Geological Society, London,
11 Special Publications 109, 197–212. doi:10.1144/gsl.sp.1996.109.01.14.
12
13
14
15
16
901 Lin, J.S., Hendricks, R.W., Harris, L.A., Yust, C.S., 1978. Microporosity
17 and micromineralogy of vitrinite in a bituminous coal. Journal of Applied
18 Crystallography 11, 621–625. doi:10.1107/S0021889878014065.
19
20
21
22
23
904 Liu, H.H., Rutqvist, J., 2010. A new coal-permeability model: internal
24 swelling stress and fracture-matrix interaction. Transport in Porous Media
25 82, 157–171. doi:10.1007/s11242-009-9442-x.
26
27
28
29
30
907 Masoudian, M., Airey, D., El-Zein, A., 2013. A chemo-poro-mechanical
31 model for sequestration of carbon dioxide in coalbeds. Geotechnique 63,
32 235–243.
33
34
35
36
910 Masoudian, M.S., Airey, D.W., El-Zein, A., 2014. Experimental investiga-
37 tions on the effect of CO₂ on mechanics of coal. International Journal of
38 Coal Geology 128-129, 12–23. doi:10.1016/j.coal.2014.04.001.
39
40
41
42
43
913 Mazumder, S., Karnik, A., Wolf, K.H., 2006. Swelling of coal in response to
44 CO₂ sequestration for ECBM and its effect on fracture permeability. SPE
45 Journal 11, 390–398.
46
47
48
49
916 Morcote, A., Mavko, G., Prasad, M., 2010. Dynamic elastic properties of
50 coal. Geophysics 75, E227. doi:10.1190/1.3508874.
51
52
53
54
918 Nikoosokhan, S., Vandamme, M., Dangla, P., 2012. A poromechanical model
55 for coal seams injected with carbon dioxide: from an isotherm of adsorption
56
57
58

- to a swelling of the reservoir. *Oil & Gas Science and Technology Rev. IFP, Energies nouvelles* 67, 777–786.
- Nikoosokhan, S., Vandamme, M., Dangla, P., 2014. A poromechanical model for coal seams saturated with binary mixtures of CH₄ and CO₂. *Journal of the Mechanics and Physics of Solids* 71, 97–111. doi:10.1016/j.jmps.2014.07.002.
- Okotie, V.U., Moore, R.L., 2010. Well Production challenges and solutions in a mature, very low-pressure coalbed methane reservoir, in: *Canadian Unconventional Resources and International Petroleum Conference*, 19-21 October, Calgary, Alberta, Canada.
- Oudinot, A., Koperna, G., Philip, Z., Liu, N., Heath, J., Wells, A., Young, G., Wilson, T., 2011. CO₂ injection performance in the Fruitland Coal Fairway, San Juan Basin: Results of a field pilot. *SPE Journal* 16, 864–879. doi:10.2118/127073-PA.
- Palmer, I., 2008. Failure during CO₂ injection in the field, in: *Coal-seq VI*, April 10-11, Houston, Texas.
- Palmer, I., Mansoori, J., 1998. How permeability depends on stress and pore pressure in coalbeds: A new model. *Evaluation* , 539–544.
- Pan, Z., Connell, L.D., 2011. Modelling of anisotropic coal swelling and its impact on permeability behaviour for primary and enhanced coalbed methane recovery. *International Journal of Coal Geology* 85, 257–267. doi:10.1016/j.coal.2010.12.003.

- 942 Pan, Z., Connell, L.D., 2012. Modelling permeability for coal reservoirs: A
943 review of analytical models and testing data. *International Journal of Coal*
944 *Geology* 92, 1–44. doi:10.1016/j.coal.2011.12.009.
- 945 Pan, Z., Connell, L.D., Camilleri, M., 2010. Laboratory characterisation
946 of coal reservoir permeability for primary and enhanced coalbed methane
947 recovery. *International Journal of Coal Geology* 82, 252–261.
- 948 Pan, Z.J., Connell, L.D., 2007. A theoretical model for gas adsorption-
949 induced coal swelling. *International Journal of Coal Geology* 69, 243–252.
- 950 Pekot, J.L., Reeves, S.R., 2002. Modeling coal matrix shrinkage and differ-
951 ential swelling with CO₂ injection for enhanced coalbed methane recovery
952 and carbon sequestration applications. Technical Report. Advanced Re-
953 sources International. Houston, Texas.
- 954 Pijaudier-Cabot, G., Vermorel, R., Miqueu, C., Mendiboure, B., 2011. Re-
955 visiting poromechanics in the context of microporous materials. *Comptes*
956 *Rendus Mécanique* 339, 770–778. doi:10.1016/j.crme.2011.09.003.
- 957 Pini, R., 2009. Enhanced coal bed methane recovery finalized to carbon
958 dioxide storage. Ph.D. thesis. ETH Zurich.
- 959 Pone, J.D.N., Halleck, P.M., Mathews, J.P., 2009. Sorption capacity and
960 sorption kinetic measurements of CO₂ and CH₄ in confined and unconfined
961 bituminous coal. *Energy & Fuels* 23, 4688–4695. doi:10.1021/ef9003158.
- 962 Ravikovitch, P.I., Neimark, A.V., 2006. Density functional theory model
963 of adsorption deformation. *Langmuir: the ACS journal of surfaces and*
964 *colloids* 22, 10864–8. doi:10.1021/la061092u.

- 1
- 2
- 3
- 4
- 5
- 6
- 7
- 8
- 9
- 10 965 Reucroft, P.J., Sethuraman, A.R., 1987. Effect of pressure on carbon dioxide
- 11 966 induced coal swelling. *Energy Fuels* 1, 72–75.
- 12
- 13
- 14 967 Scott, M., Mazumder, S., Jiang, J., 2012. Permeability increase in Bowen
- 15 968 Basin coal as a result of matrix shrinkage during primary depletion. *SPE*
- 16 969 *International SPE* 158152.
- 17
- 18
- 19
- 20 970 Seidle, J., Jeansonne, M., Erickson, D., 1992. Application of matchstick ge-
- 21 971 ometry to stress dependent permeability in coals, in: *SPE Rocky Mountain*
- 22 972 *Regional Meeting, Society of Petroleum Engineers*. doi:10.2118/24361-MS.
- 23
- 24
- 25
- 26 973 Shi, J.Q., Durucan, S., 2004. Drawdown induced changes in per-
- 27 974 meability of coalbeds: A new interpretation of the reservoir re-
- 28 975 sponse to primary recovery. *Transport in Porous Media* 56, 1–16.
- 29 976 doi:10.1023/B:TIPM.0000018398.19928.5a.
- 30
- 31
- 32
- 33
- 34
- 35 977 Somerton, W.H., Soylemezolu, I.M., Dudley, R.C., 1975. Effect of stress on
- 36 978 permeability of coal. *International Journal of Rock Mechanics and Mining*
- 37 979 *Science & Geomechanics Abstracts* 12, 129–145.
- 38
- 39
- 40
- 41 980 Span, R., Wagner, W., 1996. A new equation of state for carbon dioxide
- 42 981 covering the fluid region from the triple-point temperature to 1100 K at
- 43 982 pressures up to 800 MPa. *Journal of Physical and Chemical Reference*
- 44 983 *Data* 25, 1509–1596.
- 45
- 46
- 47
- 48
- 49
- 50 984 Thomsen, L., 1986. Weak elastic anisotropy. *Geophysics* 51, 1954–1966.
- 51
- 52
- 53 985 Vandamme, M., Brochard, L., Lecampion, B., Coussy, O., 2010. Adsorption
- 54 986 and strain: The CO₂-induced swelling of coal. *Journal of the Mechanics*
- 55 987 *and Physics of Solids* 58, 1489–1505. doi:10.1016/j.jmps.2010.07.014.
- 56
- 57
- 58
- 59
- 60
- 61
- 62
- 63
- 64
- 65

- 1
2
3
4
5
6
7
8
9
10 988 Viete, D., Ranjith, P., 2006. The effect of CO2 on the geomechanical
11 989 and permeability behaviour of brown coal: Implications for coal seam
12
13 990 CO2 sequestration. International Journal of Coal Geology 66, 204–216.
14
15 991 doi:10.1016/j.coal.2005.09.002.
16
17
18 992 Wang, Z., 2002. Seismic anisotropy in sedimentary rocks, part 2: Laboratory
19
20 993 data. Geophysics 67, 1423–1440. doi:10.1190/1.1512743.
21
22
23 994 Wu, Y., Liu, J., Elsworth, D., Chen, Z., Connell, L., Pan, Z., 2010. Dual
24
25 995 poroelastic response of a coal seam to CO2 injection. International Journal
26
27 996 of Greenhouse Gas Control 4, 668–678. doi:10.1016/j.ijggc.2010.02.004.
28
29
30
31
32
33
34
35
36
37
38
39
40
41
42
43
44
45
46
47
48
49
50
51
52
53
54
55
56
57
58
59
60
61
62
63
64
65